,STRESS MAPPING STUDIES ON SILICON NITRIDE CERAMIC USING A LASER RAMAN MICROPROBE,

Thesis

Submitted to

Graduate Engineering & Research
School of Engineering

UNIVERSITY OF DAYTON

In Partial Fulfillment of the Requirements for

The Degree

Masters of Science in Electro-Optics

by

Steven L. Ernst

UNIVERSITY OF DAYTON

Dayton, Ohio

August 1992

STRESS MAPPING STUDIES ON SILICON NITRIDE CERAMIC USING A LASER RAMAN MICROPROBE

APPROVED BY:

ABSTRACT

STRESS MAPPING STUDIES ON SILICON NITRIDE CERAMIC USING A LASER RAMAN MICROPROBE

Ernst, Steven L.
University of Dayton, 1990

Advisor: Dr. P. Yaney

The presence of microscopic cracks in brittle ceramics is often the source of mechanical failure. A characterization of the stress field in the vicinity of the crack tip aids in the study of the ability of the material to resist crack propagation. A laser Raman microprobe fitted with a two-dimensional array detector has been used to detect stress fields in β-silicon nitride polycrystalline ceramic specimens. Specifically, the spectral shift of the 864 cm^{-1} Raman vibrational mode of β-Si_3N_4 due to strain in the crystal was measured. The first of two studies was to map the stress gradient on the sides of two mechanically stressed silicon nitride bars in flexure stress. The second study was to measure the stress distribution in front of an indent-initiated crack under various flexure loads. The Raman shifts of the first study were related to the predicted stresses of the bar to obtain a conversion factor from Raman shift to stress. This conversion factor of 350 MPa / cm^{-1} was also used for the crack tip stress field study to convert Raman shifts to stress values. Six runs were performed with a 28 micron probe line length positioned in line with the extension of the crack tip. A spot size of two microns was used resulting in the simultaneous recording of 14 spectra along the probe line. The crack tip stress distribution was probed out to 35 microns. The stress pattern in the vicinity of the crack was found to consist of three distinct regions of stress. Behind the crack tip, a region of compressive stresses was found. In front of the crack tip, a process zone of increasing tensile stress out to ~16 microns was found. From ~16 microns and beyond, the stress magnitude declined toward zero stress. This region is determined by the linear elastic model of fracture mechanics. In addition to these studies, a computer ray trace of the spectrometer optics was performed to verify the astigmatism correction accomplished with a cylindrical lens. Spot patterns from the ray trace program showed that the correction was valid and that the final spot size was within the resolution of the detector (i.e., 23 microns square). A galvanometer scanner was designed to replace the current line illumination on the specimen. This design would permit the length and width of the area probed to be precisely controlled. The length can be increased up to ~100 microns on the specimen surface with widths down to one micron using this proposed design.

ACKNOWLEDGMENTS

I am deeply indebted to my advisor, Dr. Perry Yaney, for his patience and meticulous review of this work. My gratitude extends to Dr. Norm Hecht for supporting this work and his attention toward the studies on silicon nitride. I am also grateful to Dr. Allahyar Kangarlu for his review of the thesis and probing conversations over the last year.

I would also like to thank those in the Metals and Ceramics Division of the Research Institute who have helped me in numerous ways. I am especially grateful to Mr. Leon Chuck for the design of the bend fixture used in this work and also for his invaluable expertise on the fracture mechanics of ceramics. I would also like to thank Mr. Steve Goodrich for his work with the strain gages and the indentation of the specimens, Mr. Dale Grant for the photographs of the specimens, and Mr. Dale McCullum for his inspiring remarks.

A special thanks goes out to my friends I have made here at U.D. especially John Parish, who also provided insight into some troublesome dilemmas. I appreciate their support.

This thesis is dedicated to my family, Ameneh and Ellis Maxwell, for without their love and support the world surely would have fallen apart.

TABLE OF CONTENTS

LIST OF FIGURES

LIST OF TABLES

CHAPTER I

INTRODUCTION

In 1921 C. V. Raman, while journeying to Europe, observed the fascinating blue color of light scattering from the Mediterranean Sea, and so impressed by this, he began studying the elements of light scattering on liquids upon his return to Calcutta. In 1923, unknown to Raman, Austrian physicist A. Smekal predicted the effect of inelastic scattering of radiation into bands at frequencies shifted from the incident frequency -- the effect that would eventually bear Raman's name.[1] In the same year, Raman began pursuing an optical analog for frequency shifted components of the Compton effect. Five years later, Raman published the first photographs of the Raman spectra of benzene and toluene, irradiated with the indigo blue line (435.8 nm) of a mercury arc lamp.[2] For the discovery and subsequent work on the effect, C.V. Raman was awarded the 1930 Nobel Prize in Physics. Because the intensity of the light scattered at Raman frequencies is proportional to the incident light intensity, early applications of Raman spectroscopy were limited by the relatively weak excitation light sources until lasers became available.[3] Since that time, based on the large volume of published work, laser Raman scattering has become a powerful analytical tool to investigate a wide range of substances. Recently, for example, the Raman effect has formed the basis for studying the microscopic analysis of lichen encrustation involved in the biodeterioration of Italian renaissance frescoes,[4] and for studying the variation in water concentration in human eye lenses with age.[5]

Developed in 1974, laser Raman microprobes are used to investigate molecular vibrational phenomena of all phases of matter. It is an alternative technique to infrared absorption for assigning vibrational frequencies and complements X-ray techniques for structural and chemical characterization of a specimen.[6] The advantages over other spectroscopic techniques are narrow bandwidths, relatively simple spectra, spot sizes down to one micron, spatial mapping capability and non-destructive. It can be used to study a specimen held under a variety of conditions and almost any material can be studied.

The University of Dayton laser Raman microprobe was built in 1984-85 to study the variations in the Raman spectra of ceramics as well as other materials non-destructively.[7,8] Initially, zirconia[9,10] and silicon carbide[11] ceramics were studied and, over the last few years, the Raman mode shifts of silicon nitride (Si_3N_4) has been studied.[12] The basic configuration of the Raman microprobe is to focus the laser light onto the specimen surface with a microscope objective and to collect the scattered Raman light (as well as the reflected laser light) with the same microscope objective. In order to achieve adequate Raman signals, the laser power must be as high as possible without damaging the specimen. Ceramics are relatively poor thermal conductors, and therefore, the temperature under the laser spot can become sufficiently high to damage (eg., melt) the material. The laser power can be reduced but with a corresponding increase in measurement time.

Motivation

β-phase Si_3N_4 is the primary candidate material for a ceramic heat engine and, as such, investigations of its mechanical properties and, in particular, its fracture properties are beneficial. Typically, specimens of Si_3N_4 are subjected to destructive flexural and indentation tests to determine their fracture properties. The material usually fractures because of the presence of microscopic flaws (microcrack, pores, impurities, etc.). The existence of crack in a ceramic component (brittle material) results in stress concentration around the crack tip and a reduction in the tensile strength.[13] An interesting phenomenon occurs in ceramic specimens containing β-Si_3N_4 crystallites placed under load which permits non-destructive measurement of the amount of strain in the crystallites. That phenomenon is a mode shift in the Raman vibrational frequencies. By probing the ceramic specimen in the region in front of the crack tip, the observed Raman mode shift can be used to map the strain (stress) field in front of the crack tip and provide useful stress intensity information at sub-critical loads.

The accuracy and precision of these mapping measurements depends on the performance of the microprobe which can be inhibited by a number of factors. These include poor signal-to-noise ratio, specimen heating, insufficient filtering of the intense laser light, insufficient spectral resolution to detect mode shifts, and insufficient spatial resolution to map the stress field. Modifications to the U.D. Raman microprobe have overcome most of these factors for detecting β-Si_3N_4 mode shifts.

Goals of the Thesis

The main goal of this thesis was to explore the capability of the Raman microprobe for measuring stress fields in β-Si_3N_4 ceramics. The behavior of strained β-Si_3N_4 crystallites, which results in slight shifts of certain Raman vibrational frequencies, forms the basis for the measurements. Initially, two stress mapping profiles were carried out on the side of a β-Si_3N_4 ceramic specimen under four-point flexure. The compression-to-tension stress applied to the specimen was determined and provided a conversion of Raman shift to stress. The second measurement sequence mapped the stress field on the tensile surface beyond a crack tip. Several different loading conditions were employed to determine the stress intensity field. The details of these measurements and the analyses of the data are discussed in Chapters IV and V, respectively. Chapter II reviews the theoretical issues which were used in the analyses of the data.

The optical properties of the microprobe were characterized and improved with modifications. Specifically, the addition of an astigmatism correcting cylindrical lens was computer simulated using a paraxial ray trace program. The collection capability of the microprobe was upgraded with a holographic filter, and a proposal is presented to increase the collection signal and laser beam probe area by altering the probe design with an optical scanner. These topics are covered extensively in Chapter III.

CHAPTER II

BACKGROUND AND THEORY

The Raman Effect

In this work, the Raman effect is the basis for the characterization of stress fields in silicon nitride ceramics. Many variations of inelastic scattering of light fall under the heading of Raman scattering. Some examples are resonance Raman, coherent anti-stokes Raman, hyper and surface-enhanced Raman. The observed spectra in this thesis is based on the same effect as recorded by C.V. Raman,[14] namely the linear spontaneous Raman effect. Monochromatic light interacts with the molecules or lattice structure in the probed volume. Using photon-sensitive detectors, the interaction produces observable, inelastically scattered light at shifted frequencies (Raman) along with elastically scattered light at the same frequency as the incident light (Rayleigh). For the case of opaque materials, the Raman intensities are typically 10^{-7} less intense than the incident light[15] which is composed of mostly reflected and some Rayleigh light. The Raman frequencies in the scattered light are shifted from the incident frequency by precise values characteristic of the material. This allows any near-ultrviolet, visible or near-infrared laser to be used as a potential excitation source. The Raman spectra are due to the vibrations and/or rotations of the molecules or lattice in solids. For crystalline solids, the vibrations fall into two classes, internal and external, as defined by Sherwood.[16] Internal vibrations involve the stretching and bending of the chemical bonds in molecules or groups of atoms, while external vibrations involve "partial rotations and translations of molecules as a whole in the crystal lattice." Because of this relationship, assignment of a Raman frequency to a molecular or lattice vibrational mechanism is possible. Raman spectra can therefore be used for material identification.

This section begins with a classical approach of dipole radiation to explain the linear spontaneous Raman effect in molecules and introduces the force matrix describing molecular or crystalline vibrations. This is followed by a consideration of the quantum mechanical oscillator.

A molecule in an electromagnetic field has its charge distribution periodically disturbed by the field which results in an induced dipole moment. This induced moment due to an incident electric field E can be written as

$$p = \alpha E + \beta E^2 + \ldots \qquad (1)$$

where α and β are termed the first and second-order polarizabilities and have the units of volume and volume per unit electric filed, respectively. For small electric fields, the quadratic term and higher orders are not considered and therefore a linear approximation of the dipole moment is completely adequate.[17] It is the change in polarizability which produces Raman-active modes. The linear polarizability, α, can be split into the sum of two parts, α_0, a static polarizability, and a sum of time-periodic polarizabilities of amplitude, α_i, due to the normal frequencies ν_i of the molecule which can be written as

$$\alpha = \alpha_0 + \sum \alpha_i \cos(2\pi\nu_i t) \,. \qquad (2)$$

Normal frequencies include rotational or vibrational frequencies of a molecule or of a lattice as well as acoustic vibrations as observed in Brillouin scattering.[18] Combining Equations (1) and (2) with an oscillating electric field given as

$$E = E_0 \cos(2\pi\nu_0 t) \qquad (3)$$

yields the oscillating dipole moment written as

$$p = E_0\, \alpha_0 \cos(2\pi\nu_0 t) + E_0 \sum \alpha_i \cos(2\pi\nu_0 t) \cos(2\pi\nu_i t)\ . \qquad (4)$$

This can be expanded into terms corresponding to Rayleigh scattering written as

$$p = E_0\, \alpha_0 \cos(2\pi\nu_0 t)\ ,$$

to Stokes Raman scattering,

$$+ 1/2\, E_0 \sum \alpha_i \{\cos[2\pi(\nu_0 - \nu_i)t]$$

and to anti-Stokes scattering,

$$+ \cos[2\pi(\nu_0 + \nu_i)t]\}. \qquad (5)$$

Any measurement of the dipole moment or frequencies ν_i involves many molecules or scattering centers which results in an average over all the centers. In the case of gases, the average induced dipole moment is taken over all orientations of the molecules relative to the incident field. In a single crystal, the induced moment depends on the orientation of the crystalline axis relative to the incident field. In polycrystalline materials, for a sufficiently large illuminated area, the observed induced moment is an average taken over all the randomly oriented crystallites.

The vibrational modes of a molecule can be determined using the classical matrix treatment of vibrational systems composed of n particles or atoms.[20] For that molecule, 3n equations describe the arbitrary displacement of each atom, and that displacement is proportional to the force, F^j, acting on the j^{th} atom by the constant k_{lm}^{jk}, where j and k are the atoms involved in the displacement of direction l to m in three dimensions (x,y,z). The force equations can be written in Hooke's law form to show the contribution of all atoms on the j^{th} atom as

$$\begin{aligned} F_x^j &= - k_{xx}^{j1}x_1 - k_{xy}^{j1}y_1 - k_{xz}^{j1}z_1 - k_{xx}^{j2}x_2 - \ldots - k_{xz}^{jn}z_n \\ F_y^j &= - k_{yx}^{j1}x_1 - k_{yy}^{j1}y_1 - k_{yz}^{j1}z_1 - k_{yx}^{j2}x_2 - \ldots - k_{yz}^{jn}z_n \\ F_z^j &= - k_{zx}^{j1}x_1 - k_{zy}^{j1}y_1 - k_{zz}^{j1}z_1 - k_{zx}^{j2}x_2 - \ldots - k_{zz}^{jn}z_n \end{aligned} \tag{6}$$

The displacement of the j^{th} atom is induced by the incident wave and oscillates with simple harmonic motion of frequency, ν, written as

$$s_j = s_j^0 \cos(2\pi\nu t + \varphi) \tag{7}$$

where s_j^0 is the amplitude of oscillation and φ is a phase constant. The acceleration of the atom is

$$a_j = \frac{d^2 s_j}{dt^2} = - 4\pi^2 \nu^2 s_j^0 \cos(2\pi\nu t + \varphi) \tag{8}$$

$$a_j = - 4\pi^2 \nu^2 s_j \tag{9}$$

The restoring force on the j^{th} atom is then [20]

$$F^j = m_j a_j = -4\pi^2 \nu^2 m_j s_j \ . \tag{10}$$

The normal modes of vibration can be written as the restoring force on the j^{th} atom in x,y,z coordinates as follows:

$$\begin{aligned} F_x^j &= - 4\pi^2 \nu^2 m_j x_j \\ F_y^j &= - 4\pi^2 \nu^2 m_j y_j \\ F_z^j &= - 4\pi^2 \nu^2 m_j z_j \ . \end{aligned} \tag{11}$$

Substituting Equation (11) into Equation (6) we obtain a 3n x 3n set of equations which represents the bonding and stretching of the molecular bonds. The roots of the determinant of the resulting matrix can be used to determine the 3n-3 possible values of ν^2, the normal modes of vibration, provided the center of mass is not included and all values of k_{lm}^{jk} are known. In the case of an isotropic and homogeneous medium with one kind of atom, all force constants but k_{xx}^{jk}, k_{yy}^{jk} and k_{zz}^{jk} are zero. The non-zero constants reduce to

$$k_{xx}^{jk} = k_{yy}^{jk} = k_{zz}^{jk} = k^j \ . \tag{12}$$

Then the force equation becomes

$$F_x^j = - k^j x = -4\pi^2 \nu^2 m_j x_j \quad , \tag{13}$$

which leads to the classical oscillator result

$$\nu = \frac{1}{2\pi} \sqrt{\frac{k^j}{m_j}} \ . \tag{14}$$

The normal vibrations of bent and linear XY_2 molecules are shown in Figure 1 as a schematic representation of the relative displacements of the atoms, X and Y.

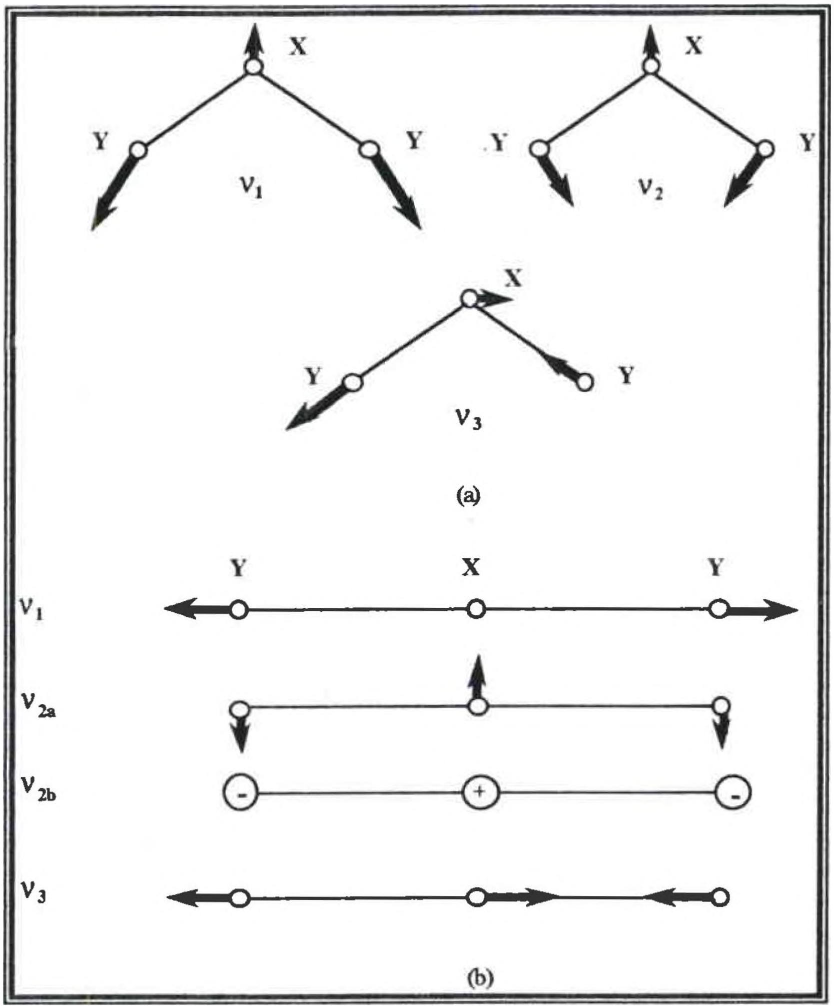

Figure 1: Normal vibrations of a bent (a), and a linear (b) XY_2 molecule.

For the case of the linear molecule, the vibrations, ν_{2a} and ν_{2b}, occur in the plane of the paper and perpendicular to it and are, therefore, equal. That vibration is considered doubly degenerate. For the bent molecule, Figure 1(a), all three modes shown involve a displacement of the center of positive charge from the center of negative charge during the vibration, which results in infrared activity, as well as a change in polarizability (i.e.

volume), which results in Raman activity. However, for the linear molecule in Figure 1(b), only v_1 is Raman active from the same reasoning. These normal vibrations are typical of Raman and infrared modes. In general, there can be modes which are inactive relative to both Raman and infrared processes.

Similar to the classical model, a quantum mechanical oscillator model can be set up which considers the vibrational modes as energy levels in terms of the classical coordinates.[19] Group theory can be used to find the symmetry properties of the wave functions and define which modes are active and inactive. For incident light of frequency, v_o, the energy diagram in Figure 2 illustrates the difference between Stokes, anti-Stokes, and Rayleigh scattering.

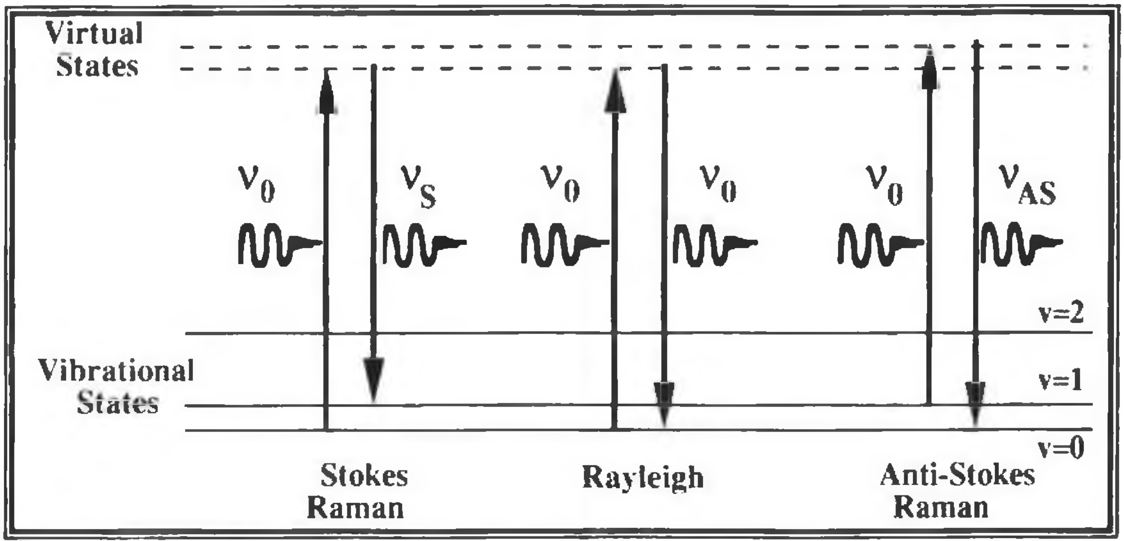

Figure 2: Energy level diagram for Raman and Rayleigh scattering.

Photons colliding with molecules in a low-lying state, such as the ground state scatter elastically at the same frequency (Rayleigh) or inelastically at a lower Stokes frequency $v_s = v_0 - v_i$, where v_0 is the frequency of incident light and v_i are the same normal vibration frequencies of the molecule described in Equations (2) through (5). They are represented in Figure 2 a vibrational states (v = 1, 2, . . .). If the molecule is in a higher vibrational state initially, the inelastically scattered frequency can be up-shifted to $\nu_{as} = \nu_0 + \nu_i$, and is known as anti-Stokes Raman scattering. Intensity differences between Stokes and anti-Stokes scattering occur because of the population distribution of the molecules iacross the vibration states. At room temperature, more molecules are in the ground state and, therefore, it is more likely that incoming light will interact with these molecules.[20]

In summary, the total power scattered in all directions for Rayleigh scattering depends on the second derivative with respect to time of the induced moment, Equation (1), and is given by[21]

$$P = \frac{8\pi^3 \nu^4}{3\varepsilon_0^2 c^4} N \alpha^2 I \tag{13}$$

where N is the number of scattering centers and I is the incident irradiance of frequency ν. This equation is also a good representation of Raman scattering for both molecules and solids where α is the polarizability for the vibrational mode which involves the wave functions of the transition states corresponding to the scattered frequency ν_s (assuming $\nu_s = \nu$.

Strain-Induced Raman Mode Shift

Deformations, in the form of strain in a crystal, may alter the Raman spectra in the following ways: 1) the generation of additional frequencies due to a lowering of crystal symmetry; 2) intensity variations of the modes; 3) shifting or splitting of modes.[22] Strain in a crystal occurs in a number of situations for which changes in the characteristic Raman spectra have been used as an investigative tool. In semiconductors, strain occurs due to a general class of defects called edge defects. They include mismatches of crystal parameters (lattice spacing, thermal expansion coefficients) at epitaxial boundary layers.[23] As another example, polishing of sapphire and silicon induces strain in the surface crystals.[24] These types of strain are built-in to the lattice and are sometimes referred to as intrinsic or residual strain.

Externally applied stress also induces strain in a material according to the equation

$$\sigma = E\varepsilon \ , \tag{14}$$

where σ is the bulk stress due to mechanical loading in MPa, E is Young's modulus expressed in MPa, and ε is the strain in the material and is dimensionless. Both the stress and strain are, in general, second-rank tensors. A bent bar under elastic conditions exhibits this relation. However, foreign inclusions, pores and cracks, classed as flaws in a material, may contain a concentration of stress or residual stress especially very close to the flaw.[25] For a polycrystalline material, the crystallites in the stress field exhibit a residual strain. Research in semiconductor strain provides much information on crystalline strain effects including the equation relating the strain and stress to Raman mode shift given by[26]

$$\frac{\Delta\nu}{\nu_0} = D\frac{\Delta V}{V_0} \cong D\varepsilon \tag{15}$$

which relates the change in crystal volume ΔV to the shift in vibration frequency, $\Delta\nu$, by a proportionality constant, D which depends on crystal and strain parameters. Data and results of Raman mode shifts for β-silicon nitride ceramic specimens can be found in Chapters IV and V.

Silicon Nitride

Since the late 1960's, silicon nitride (Si_3N_4) has been considered a candidate material for various components in advanced heat engines,[27] as well as for other high temperature and corrosive environments, because of its combination of high strength and high thermal conductivity, low thermal expansion and good high-temperature stability. Another use of Si_3N_4 is as amorphous thin films for insulation passivation layers on integrated circuit chips.[28]

Crystalline silicon nitride exists in two polymorphs, $\alpha-Si_3N_4$ and $\beta-Si_3N_4$. The β-phase is the more stable phase because at high temperatures the α-phase crystals are converted (densified) to β-phase. The Si_3N_4 investigated in this study is predominately $\beta-Si_3N_4$. The crystalline structure of $\beta-Si_3N_4$ is hexagonal with dimensions a = 7.606 Å and c = 2.909 Å and its space group is C_{6h}^{2} ($P6_3/m$). The atomic structure of $\beta-Si_3N_4$ is shown in Figure 3. Its unit cell contains 14 atoms .

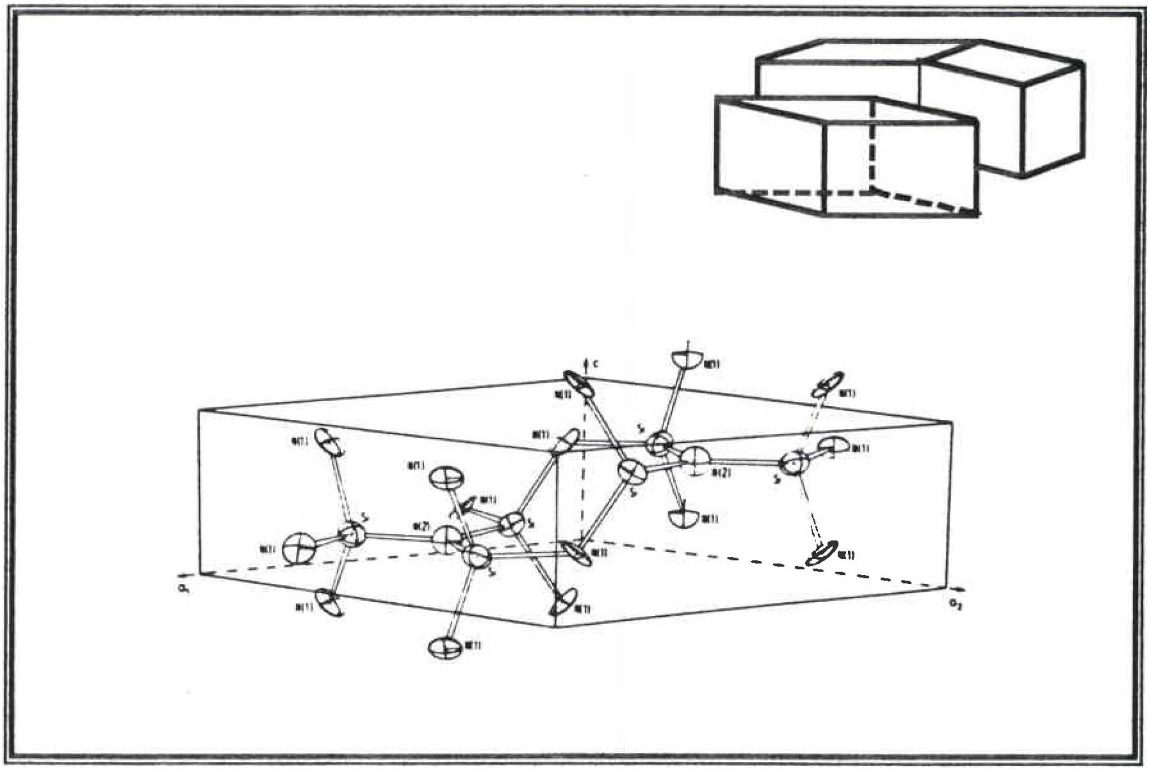

Figure 3: Atomic structure of the $\beta-Si_3N_4$ unit cell, including some nitrogen atoms from neighboring cells. (Taken from Reference 29.)

The vibrational modes of β–Si_3N_4 have been calculated by Wada and others[30] using group theory, but the modes have not been assigned to the observed spectra. The acoustic and optical modes are

$$\begin{aligned} \Gamma_{acoustic} &= A_u + E_{1u} \\ \Gamma_{optical} &= 4A_g\,(R) + 3B_g + 2E_{1g}\,(R) + 5E_{2g}\,(R) \\ &\quad + 2A_u\,(IR) + 4B_u + 4E_{1u}\,(IR) + 2E_{2u}\,. \end{aligned} \tag{16}$$

There are 11 active Raman (R) and six active infrared (IR) modes. Of the 11 observed Raman modes four are presumed external or lattice modes because of their low frequencies.[31] Ten of the 11 Raman modes observed with the U.D. microprobe are shown in Figure 4.

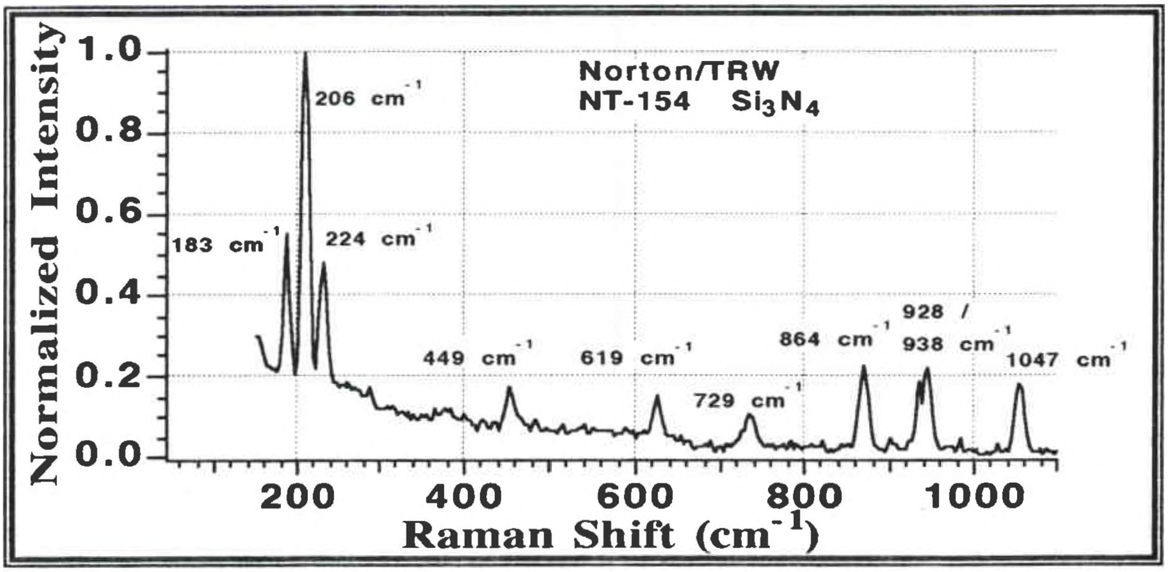

Figure 4: Raman spectrum of β-Si_3N_4. (Taken from Reference 32.)

The 864 cm^{-1} internal mode has been singled out for strain-induced mode shift studies because it has the highest intensity of the internal modes and shifts more than the other internal modes.[32]

β–Si_3N_4 and α–Si_3N_4 do not exist naturally and the forming process and additives used affect the polycrystalline structure and, therefore, its strength and temperature properties. The ceramic used in this thesis is Norton/TRW NT-154 $\beta\text{-Si}_3\text{N}_4$. It is a HIP'ed (hot isostatic pressed) material with 4% yttria as a sintering aid. The microscopic structure consists of randomly-oriented, elongated crystallite grains of $\beta\text{-Si}_3\text{N}_4$ in a glassy matrix containing Y_2O_3 and SiO_2. The crystallites have a diameter of 1 - 2 µm with a long dimension of approximately 4 - 9 µm. A scanning electron micrograph of an etched sample of NT-154 $\beta\text{-Si}_3\text{N}_4$ is shown in Figure 5.

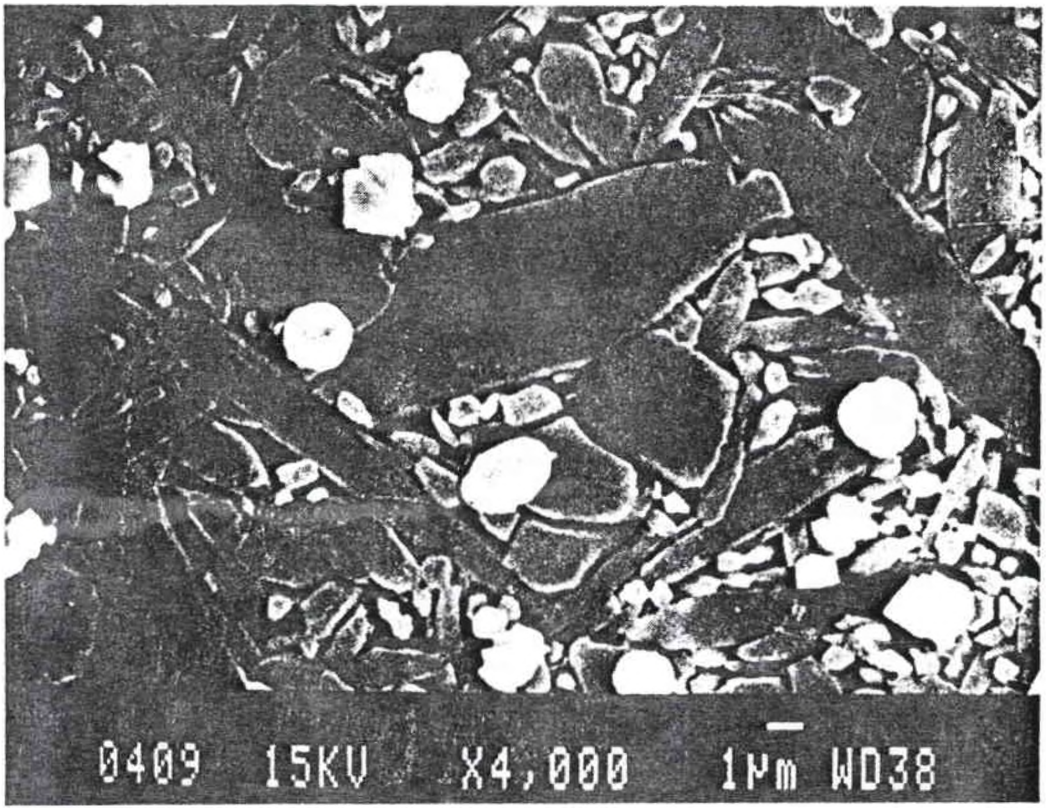

Figure 5: SEM of $\beta\text{-Si}_3\text{N}_4$ showing the random sizing and orientation of the elongated crystallite grains. (Taken from Reference 33).

The yttrium oxide in the glassy phase surrounding the $\beta\text{-Si}_3\text{N}_4$ grains has been mostly etched away. The white granules are Y_2O_3 residue from the etching process. The very small grains are unconverted α-phase silicon nitride. It has been proposed that the dark grey color of commercial Si_3N_4 (absorbs visible light) is due to the total internal reflection and refraction of light at the crystallite boundaries into the material[34] and/or small amounts of iron impurities (<100 ppm) in solution with the Si_3N_4 lattice.[35] Silicon nitride powder suppliers guarantee impurities <100 ppm.[36]

Silicon nitride, in general, have superior physical and mechanical properties at elevated temperatures compared to metals; however, as a ceramic, brittle material, it is subject to low fracture resistance. The strength-limiting defects found in the volume of NT-154 Si_3N_4 are metallic inclusions. Surface flaws, namely pores, foreign inclusions, and cavities formed by a lack of yttria, dominate microscopic evaluation of flexural test specimens.

Stress and Strain in Ceramics

The study of microscopic strain by observing the shift in a characteristic Raman mode may be correlated with a macroscopic event. For the ceramic specimens investigated in this study, the macroscopic event is an applied load and a crack caused by an indent. Two studies were performed relating a measurable load with the microscopic strain measurement. The first was a study of the stress distribution on the side of a loaded beam (specimen) in a four-point bend fixture from its tension surface to the compression surface. The second was the study of the stress distribution directly ahead of a crack. Since a failure in any solid, ceramic or otherwise, begins with the propagation of a flaw under load, this study is of considerable importance, and forms the basis of fracture mechanics.

Tension-to-Compression Stress Distribution

A four-point flexural fixture transfers an applied bending moment to a test beam. This yields a uniform tensile stress between the inner span of the fixture on the top face of a bar as shown in Figure 6. The bottom face experiences a compressive stress equal to the tensile surface stress. Single-dimension moment arm analysis can be used to determine the stress distribution throughout the beam.

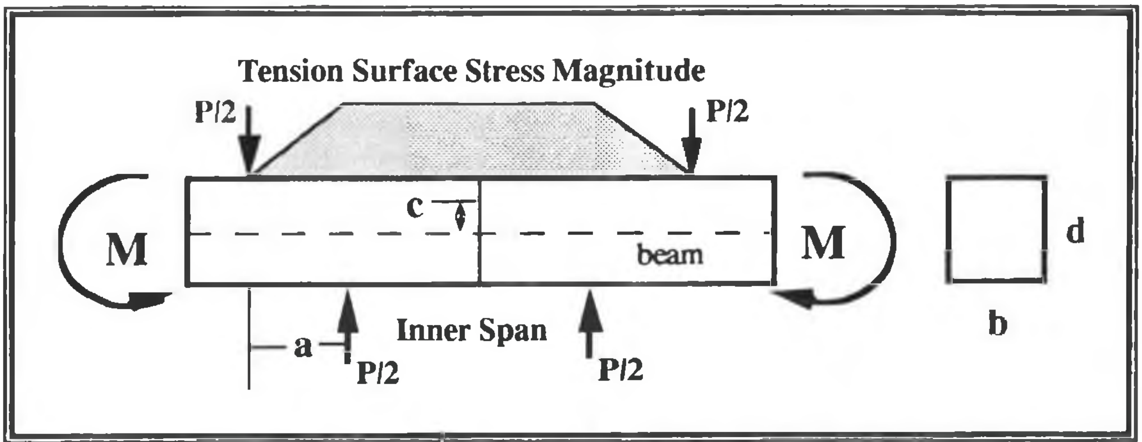

Figure 6: Tensile stress of a beam in four-point flexure. The surface stress is uniform between the inner span loading points.

Following the analysis given by Shigley,[37] the general flexure stress formula is given as

$$\sigma = \frac{Mc}{I} , \qquad (17)$$

where M is the moment, c is the distance from the neutral axis, and I is the area moment of inertia. The neutral axis for a rectangular solid is a plane that lies in the center of the beam, parallel to the maximum stress surfaces and where the stress due to the applied load is zero. The stress for a rectangular beam is then

$$\sigma = \frac{6\ \mathrm{Pac}}{\mathrm{bd}^3} \tag{18}$$

where P is the applied load, and the maximum stress is given by

$$\sigma_{\max} = \frac{3\mathrm{Pa}}{\mathrm{bd}^2}\ . \tag{19}$$

The stress distribution[37] is shown graphically in Figure 7.

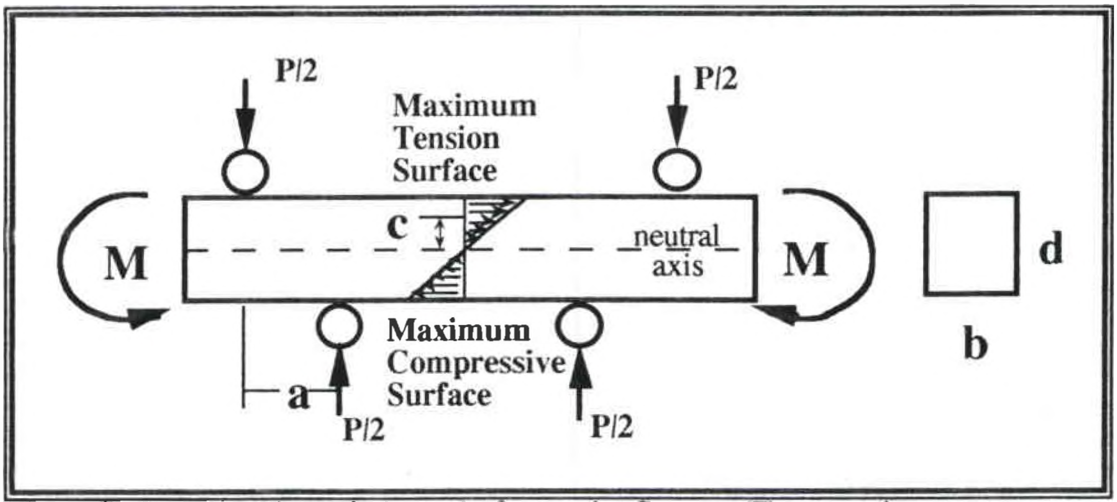

Figure 7: Stress gradient of a beam in four-point flexure. The stress is zero at the neutral axis.

Crack-Tip Stress Distribution

The strength properties of the rectangular beam are determined by its response to loading conditions. The strength of ceramic materials is generally characterized by flexural testing.[38] The flexural strength is the maximum tensile stress calculated by Equation (19) when subjected to a critical applied load resulting in fracture of the beam. The flexure strength of the material depends on many parameters, but in particular, it depends on the manifestation and size of a critical flaw in the bar. The flaw is the origin of the fracture.

The discussion so far considers only the bulk characteristics of the material.

However, because of the effect of flaw size on the flexural strength, the stresses near the flaw must also be considered. For the case when the flaw is a crack, fracture mechanics can be used to predict the magnitude and distribution of the stress near the tip of the crack. The fundamental principle in fracture mechanics is that the stress magnitude ahead of the crack is intensified and can be characterized by the stress intensity factor K. The stress is not limited to the tip of the crack but is distributed well beyond the tip, and is referred to as the stress field. Under load, the stress at the tip increases until the material deforms and the crack propagates to relieve the stress at the tip. The deformation of the material can be separated into three modes based on the applied stress direction: mode I, the opening mode; mode II, the sliding or shearing mode and; mode III, the tearing mode. Mode I is most often encountered in ceramics[38] and is the mode for a tensile bend test with four-point flexure. The tensile stress applied is perpendicular to the crack, and the stress intensity for mode I is denoted K_I expressed in $MPa{\cdot}m^{1/2}$. For a linear elastic and isotropic material the stress in front of a crack is given as[39]

$$\sigma = \frac{K_I}{\sqrt{2\pi r}} \cos\frac{\theta}{2}\left(1 + \sin\frac{\theta}{2}\sin\frac{3\theta}{2}\right) + \text{higher-order terms} \tag{20}$$

where r and θ are the polar coordinates from the crack tip. Directly ahead of the crack, where $\theta = 0$, and for small distances r, the higher-order terms can be neglected.[40] The observed stress is related to the stress intensity K_I and is inversely proportional to the square root of r, and is written as

$$\sigma = \frac{K_I}{\sqrt{2\pi r}} \tag{21}$$

The stress intensity factor K_I is proportional to the crack length, specimen geometry and the applied stress according to the equation

$$K_I = \psi \, \sigma_a \sqrt{c} \tag{22}$$

where the factor ψ represents the crack shape and specimen geometry, σ_a is the applied stress, and c is the flaw size. For these studies the crack was formed using a diamond indent on the surface of a silicon nitride beam. The impact of the diamond creates a so-called half-penney crack morphology with cracks extending out from the corners of the indent. An isometric section of the crack morphology is shown in Figure 8. The shaded region in Figure 8 indicates fractured areas and the cross-hatched region indicates permanent deformation of the ceramic. The indent size compared to the specimen in Figure 8 has been enlarged to illustrate the crack geometry.

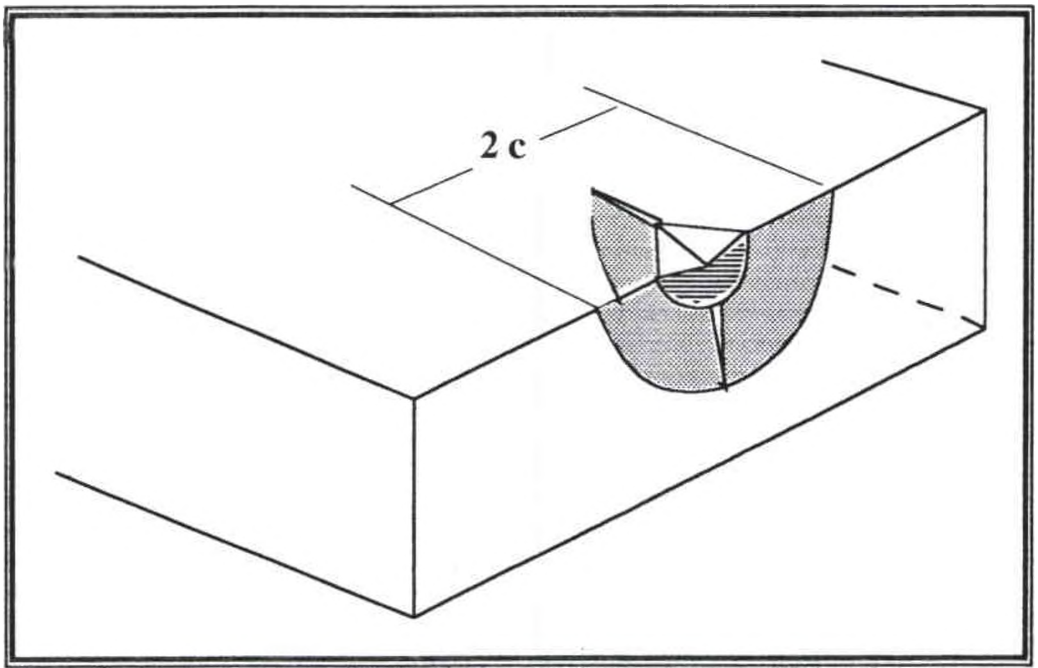

Figure 8: Isometric view of half-penney crack morphology. (Taken from Reference 41.)

For a half-penney crack the geometrical factor is[42]

$$\psi = \frac{2}{\sqrt{\pi}} \tag{23}$$

Consequently, according to Equation (21), the applied stress, the crack size, shape, orientation, and the material properties affect the value of K_I but do not alter the stress field relationship with r. From Equation (22) the stress intensity is directly related to the applied stress or load. If a critical load is applied, the crack propagates in an unstable mode until the bar is completely fractured. The stress intensity factor then equals a critical stress intensity, K_{IC} and is defined as the fracture toughness written as

$$K_{IC} = \psi\, \sigma_{cr} \sqrt{c} \tag{24}$$

where σ_{cr} is the critical applied stress which leads to unstable fracture. The fracture toughness is determined by destructive methods. Typically, a material is indented to produce a flaw of known size and is subjected to a critical stress which causes fracture. The fracture toughness represents the inherent ability of a material to resist crack propagation.[43]

An extension of the linear elastic fracture mechanics model of crack-tip stress with the incorporation of the polycrystalline microstructure of some ceramics is proposed by Fairbanks and others.[44] The silicon nitride material used in this investigation is polycrystalline with yttria in the grain boundary phase. Consequently, silicon nitride is not isotropic and not homogeneous. Fairbanks and others propose that the stress intensity factor found in ceramics is not limited to only the applied load and crack geometry. The stress intensity is also related to the indentation parameters involved in the crack formation and the material microstructure interaction with a propagating crack. The total stress intensity factor is a superposition of stress intensity factors written as

$$K = K_a + K_r + K_m \qquad (25)$$

where K_a is the previously discussed stress intensity factor defined by Equation (22), K_r is a residual factor due to the indentation and K_m is a crack-microstructure interaction factor. According to Fairbanks and others, the incorporation of K_m provides for an analytical background to consider the effect of naturally occurring flaws on the fracture toughness. The residual stress intensity due to the indentation process is not only a function of the flaw length, but also the initial indentation load P_r, written as

$$K_r = \chi P_r c^{-3/2} \quad . \qquad (26)$$

where χ is a residual contact field parameter.[44] While the details of the analysis of the additional stress intensity factors K_r and K_m are beyond the scope of these studies with β-silicon nitride, it is necessary to consider the possible contribution of these terms, especially since K_a alone is based on the assumption of an isotropic and homogeneous material.

A final modification to the crack-tip stress distribution arises from the apparent discrepancy of the stress very close to the tip. Equation (21) predicts that the stress approaches infinity at the crack tip. This obviously cannot occur for any material. To illustrate this, Figure 9 shows the stress intensity for two hypothetical stress intensity factors, $K_I^{(1)}$ and $K_I^{(2)}$, where $K_I^{(2)} > K_I^{(1)}$. Since the material cannot sustain such a high stress intensification near the crack tip some other condition is involved. For a homogeneous material, the region very close to the crack tip undergoes some deformation, creating a process zone where the material no longer behaves elastically.[45] The idea of a process zone in the material can be viewed as a necessary intermediate stress condition between the linear elastic behavior of the material and rupture. The size of the zone depends directly on the stress intensity factor K_I and the intrinsic yield stress of the material, σ_y. Consequently, Equation (21) defines the stress field for which r > process zone distance and, therefore, $\sigma < \sigma_y$. The process zone boundary distiguishes the stress field which follows the linear elastic theory (the K-dominated zone) and the stress field of the process zone.

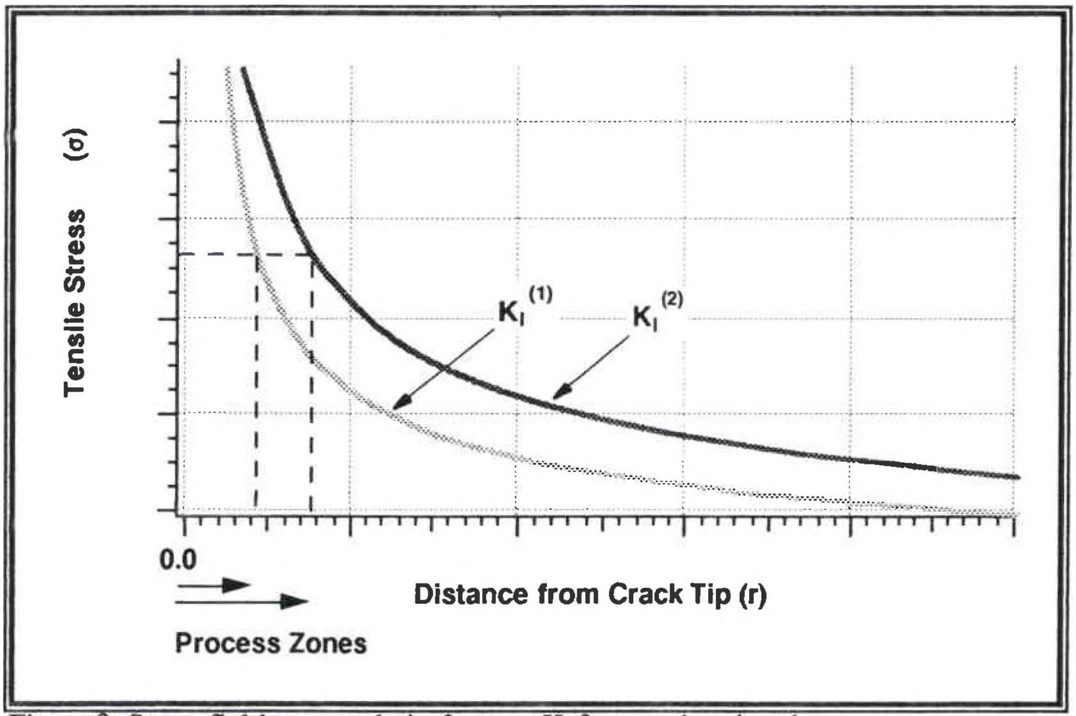

Figure 9: Stress field at a crack tip for two K-factors showing the process zones.

In Figure 9, the yield stress defines a process zone for each stress intensity factor. The curves also show that well beyond the tip, in the K-dominated zone, for a given distance where r > process zone size, the magnitude of stresses are different with respect to the stress intensity factor. As stated before, these curves are based on the stress intensity factor K_I. Consequently, the crack-tip stress distribution may be characterized by the process zone size and the magnitude of stress in front of the tip and not, generally, by its maximum stress value. Again, the process zone discussion is based on an isotropic and homogeneous material; however, silicon nitride may not meet these rigid criteria. The infinite stress limitation on linear elastic theory is valid with silicon nitride and some characteristic σ_y exists which defines a finite distance beyond the crack tip over which the stress pattern does not adhere to the K-dominated zone stress intensity.

In summary, fracture mechanics can predict the stress distribution in the vicinity of a crack tip in an isotropic and homogenous material. Central to the characterization of the crack-tip stress is the stress intensity factor, the parameters of which relate macroscopic events to the stress distribution. Where applicable, the linear elastic theory was modified to incorporate the realities of polycrystalline ceramics like silicon nitride. Chapter V extends the ideas of this section to analyze the data obtained in this investigation.

CHAPTER III

MICROPROBE DESIGN AND MODIFICATIONS

The Raman microprobe used for these studies was originally designed and built in 1984-1985 by Dr. Yaney and Dr. Schneider along with then graduate student Mr. Michael Wager.[7] Five graduate students[8-12] have worked on the system in the intervening years with each modifying and upgrading the microprobe to accomodate the ceramic being studied and to incorporate more efficient means of detecting the Raman signals. This chapter describes the optical setup used to obtain the spectra in this thesis. An overview of the computer ray trace performed to characterize and correct the astigmatism inherent to the spectrometer is presented. This is followed by a discussion of the addition of a holographic edge filter to improve the optical throughput at Raman frequencies. Finally, the design and benefits of a scanning illumination scheme are presented.

Microprobe System

A diagram of the setup used is shown in Figure 10. The system can be split into an illumination design and a collection design. The source of the probing laser light is a Chromatix Nd:YAG laser operating in the Q-switched, frequency doubled, burst mode and tuned to 532 nm. The spectral bandwidth is 1 cm^{-1}. The pulses generated are typically bursts of 7-10, 150 ns Q-switched pulses for each 120 microsecond lamp flash operated at ~58 Hz. The power output is averaged and detected with a thermal Scientech 362 Power/Energy Meter located after mirror M2. The typical average power of the laser ranges from 30 mW to 65 mW, depending on the age of the lamp, for an applied lamp voltage of 340 volts. With age the lamp efficiency decreases which limits the number of Q-

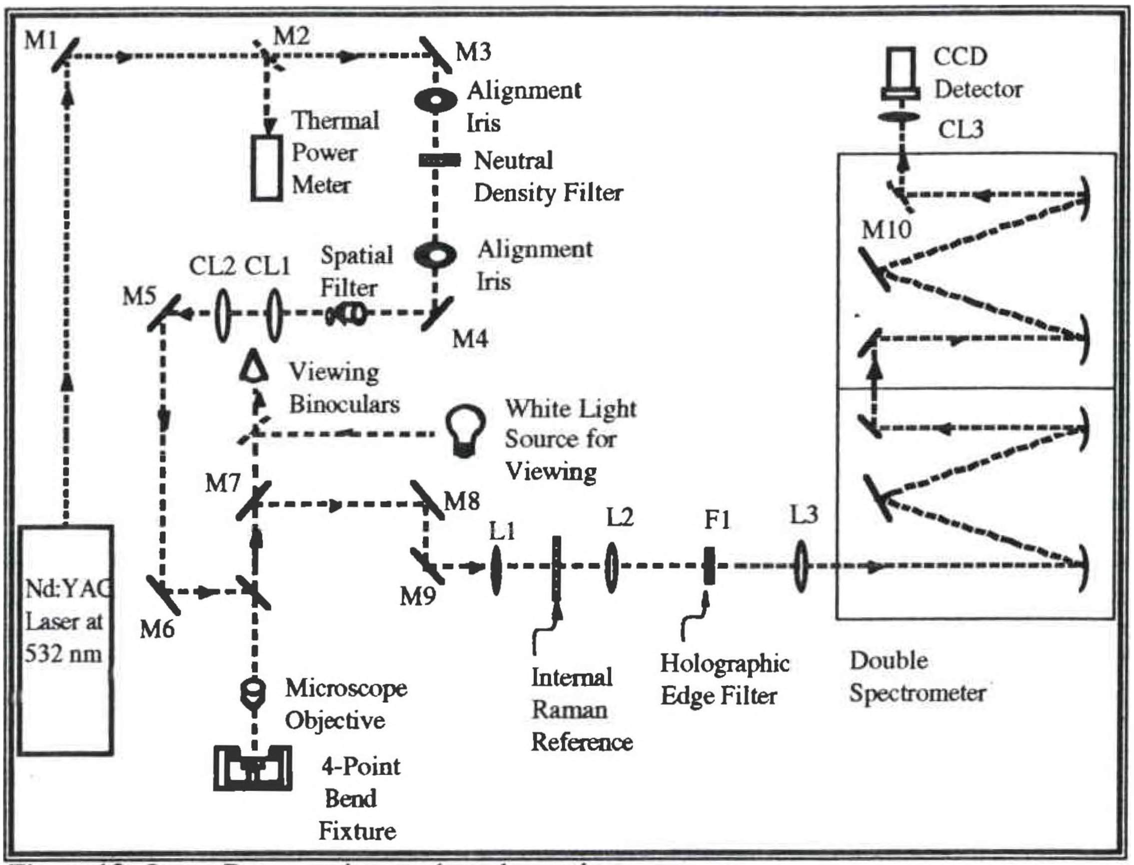

Figure 10: Laser Raman microprobe schematic.

switched pulses which fit into a single lamp pulse and thereby lowers the average power. Mirrors M1 and M3 align the laser beam parallel to the table and irises I1 and I2 provide for easy realignment if the beam becomes misdirected. The beam is attenuated by a neutral density filter usually set at 0.65 for these studies. The attenuation provided by this filter plus the transmittance of the following optics results in average power levels at the specimen of 0.70 mW to 0.94 mW. The beam is then directed into a cylindrical lens/spatial filter assembly. The diverging beam from the pinhole aperture is collimated in the vertical plane by a 15 mm focal length cylindrical lens CL1, and in the horizontal plane by a 40 mm focal length cylindrical lens CL2. The beam shape is no longer circular but is extended to an elliptical shape. The beam is directed up and horizontally, respectively, by mirrors M5 and M6 to a 70/30 beamsplitter which transmits 30% of the laser light down into a Nikon M-Plan 60x extra-long-working-distance microscope objective. The focused probe beam on the specimen surface is a line image with Gaussian intensity profiles in both dimensions. When the 15 mm cylindrical lens is defocused, the beam is no longer collimated in the vertical plane so that a diverging wavefront is incident on the microscope objective. This results in a lengthening of the line image on the specimen surface. This effectively reduces the specimen heating problem because the beam is spread over a larger specimen area and offers an added advantage of collecting scattered signal from a larger probe area.

The microprobe's collection system involves imaging and dispersing the light from the probed area onto the detector. The scattered light from the specimen consists of Raman, Rayleigh and reflected light. The light travels back through the objective with 70% transmitted through the beamsplitter. For the case when the 864 cm^{-1} mode of Si_3N_4 is being observed, a quartz cuvette of nitromethane is placed at the focal plane between two 200 mm focal length achromatic lenses (L1 and L2 in Figure 10). Nitromethane strongly scatters a Raman mode at 915 cm^{-1} which provides a suitable reference from which shifts of the 864 cm^{-1} mode can be measured. The light is then filtered by F1 which is either a sharp-cut colored glass filter (Corning C.S. No. 3-67) or a Physical Optics Corp. RHE 532.1D holographic edge filter tuned to reject light at 532 nm. These filters block the Rayleigh and reflected light while passing the Raman frequencies to the spectrometer. The specifications of the holographic filter are listed later in this chapter. A 50 mm camera lens focuses the light onto the entrance slit of the Spex 1401 double spectrometer. The double spectrometer has a focal length of 0.85 m and uses two 1200 grooves/mm reflection gratings blazed at 500 nm as the dispersing elements. Two methods of detection are configured into the microprobe. For single-channel PMT detection, the light passes through a third monochrometer coupled to the exit slit of the double spectrometer. The second method was used for all measurements presented in this thesis. It is multi-channel detection using a liquid-nitrogen-cooled Princeton Instruments CCD two-dimensional array detector which permits simultaneous measurement of a range of wavelengths. A flip mirror inside the double spectrometer located just before the exit slit directs light to the array detector mounted on the side of the spectrometer. The spectral range of the detector is determined by the middle slit width of the double spectrometer, which is opened to its maximum of 3 mm. The array detector simultaneously detects up to a range of 83 cm^{-1} which corresponds to 250 pixels. Furthermore, to be functional in both dimensions the spectrometer must *image* the entrance slit onto the array detector. Initially, this was not possible because of the astigmatism due to the off-axis spherical optics of the spectrometer. This aberration, which is not a problem with the single-channel method, was corrected using a 150 mm focal length cylindrical lens, CL3, located between the flip mirror and the array detector. The line image on the specimen is focused on the array detector in the vertical direction while the spectral axis is focused along the horizontal direction.

The detector is 384 pixels high (spatial dimension) by 578 pixels wide (spectral dimension) with each pixel measuring 23 x 23 μm^2. The detector comes with software which allows acquisition of spectra in a variety of methods. Most notably is the binning capability which allows the individual pixels to be grouped together to form a super-pixel.[46] Binning increases the signal-to-noise ratio simply because of the larger area in which it accumulates charge. Binning also reduces the number of pixel read-out operations lowering the total detector noise. For a super-pixel comprised of a one-pixel-wide vertical strip, the detector maintains its full spectral resolution while combining the photo-electrons generated by the light on the super-pixel. This method of binning is used for the case when the spatial information along the probe line is inconsequential. Otherwise, each pixel can be resolved and no binning is used in the acquisition. With the 60x microscope objective, a single vertical pixel on the detector corresponds to two microns on the specimen surface, and the effective probe beam area is ~2 microns by ~28 microns which corresponds to 14 vertically-aligned pixels on the array detector. For the studies measuring the silicon nitride 864 cm^{-1} mode shift,this mode and the nitromethane reference Raman mode at 915 cm^{-1} are imaged onto the detector array. Upgraded software from Princeton Instruments allows on-screen 3-D display of the array. The software also comes with data and image processing routines. The most commonly used post-processing routine is the cosmic-ray-induced-artifact removal. Cosmic rays can overwhelm spectral features when the detector is operated with long exposure times and many pixels are binned.

The specimen surface can be viewed with the aid of a white light source through a pair of binoculars configured within the collection design as an auxiliary setup. This allows the laser beam to be visually focused and positioned on the specimen surface. A sharp-cut red glass filter (Corning C.S. No. 3-66) located just before the binoculars provides a suitable attenuation of the intense laser beam into the viewer's eyes. A flip prism inside the binocular housing directs the image of the specimen surface to a video camera for viewing on a small TV screen. Removing the red filter improves the visual contrast of the specimen surface which is necessary sometimes to locate minute specimen structures, flaws, or cracks. However, the laser beam must be turned off to protect the viewer's eyes or the camera's detector element from the intense reflected laser light.

The specimen holder is a four-point bend fixture as shown in Figure 11. The outer span and inner span dimensions are 40 mm and 20 mm respectively, and designed to uniformly load a ceramic specimen bar of dimensions 3 mm x 4 mm x 50 mm. The specimen is loaded by tightening the nut at the bottom which puts pressure on the inner span platform. The contact points to the specimen are four rods each in their own V-groove to prevent slipping. The fixture can be placed upright for applications involving a uniform tensile stress field at the top surface of the specimen or on its side for varying strain field applications. The original design of the fixture was for the upright position. In order to use the fixture on its side, the inner span platform was trimmed down to the size of the specimen, ~4 mm, along with all the contact rods. This allowed room for the microscope objective. A final modification was to drill shallow holes in the side of the 7/8 inch tightening nut. A small rod inserted in any one of the holes is used to tighten the nut and load the specimen.

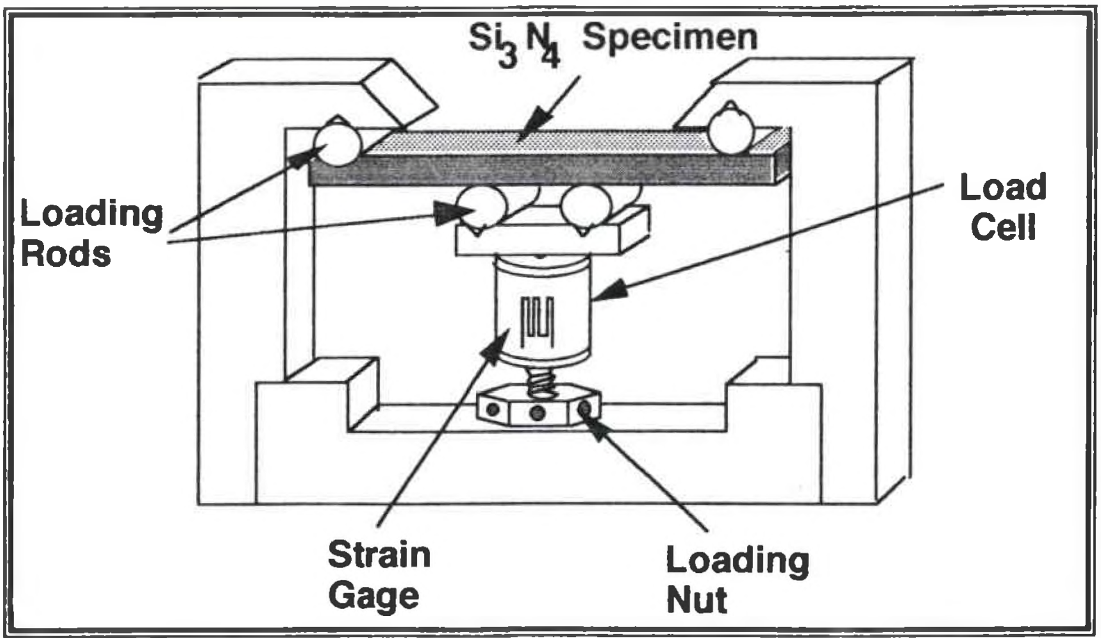

Figure 11: Four-point bend fixture used to load silicon nitride specimens. The strain measurement from the load cell is used to determine the load on the bar.

Computer Ray Trace Model of Astigmatism Correction

The Spex model 1401 double spectrometer, which is based on the Czerny-Turner design, contains collimating and focusing spherical mirrors located in off-axis positions. This design naturally suffers from astigmatism. Of the two focal planes established, the tangential focus is defined as the convergence of rays with angles only along the horizontal plane and the sagittal focus occurs where rays in the vertical plane converge. A 150 mm focal length, plano-convex, cylindrical lens was placed in front of the CCD array detector to bring the sagittal focus into the tangential focus. The second-half of the double spectrometer is illustrated in Figure 12. The first half is nearly identical to the second half.

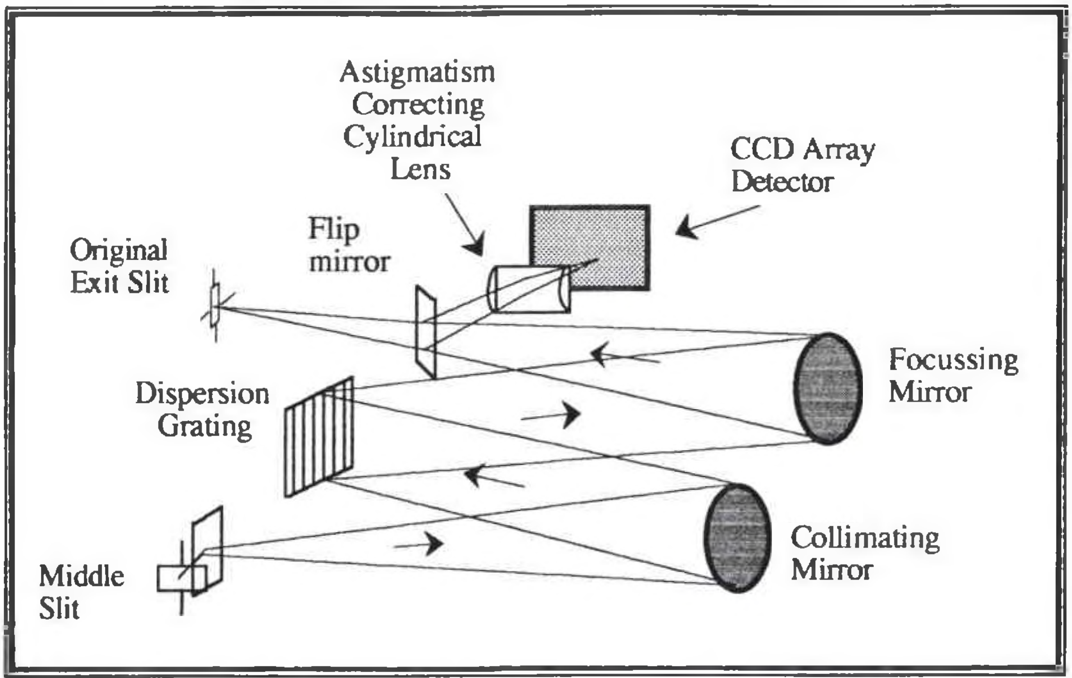

Figure 12: Second-half of the double spectrometer. The arrows show the direction of the light through the system (the optic axis).

The astigmatism and the correction of it was verified visually and experimentally with spectra obtained from the array detector by Yaney and Blackshire.[12] An entrance slit image of neon light measuring 10 microns wide by ~25 microns high provided spatial (vertical) and spectral (horizontal) focus information. The intensities of both the 16462.8 cm^{-1} (607.43 nm) and the 16403.7 cm^{-1} (609.62 nm) emission lines were each observed to peak on one 23 μm pixel and drop significantly at vertically adjacent pixels. The emission lines were not detected just two pixels away from the peak indicating a sharp focus in the spatial dimension. The spectral focus was determined by the full width at half maximum (FWHM) of each emission line. The FWHM measured 2-3 pixels indicating a sharp focus in the horizontal dimension. Other studies performed to determine the focusing ability of the system showed the spectral focus to be 1-2 pixels. Nonetheless, the theoretical spot size of the system remained unknown. To determine this size and validate the astigmatism correction, the optical system of the spectrometer, from the entrance slit to the detector plane, was modeled with the computer ray trace program, Beam Four, on an IBM-PC.[47] Only the highlights and peculiarities of the modeling process are presented avoiding the details of the program.

The program modeling operates under the assumption of paraxial ray tracing and therefore an ideal point source is possible. Beam Four can model the entire spectrometer, including the dispersion of the gratings. Because the spectrometer was fitted with the CCD detector on the side of the spectrometer, the positions and angles of the components were initially aligned to focus at the original exit slit. To model the spectrometer, initial measurements were made of the path lengths and the mirror and grating positions. The exact angles and positions were optimized using the autoadjust feature of the program.

The autoadjust feature works with the user-specified rays to adjust the dimension, angle and position of any optical element or elements in the system for a minimum RMS blur diameter of the final ray positions. It is a Gauss-Newton, non-linear, iterative, least-squares optimization routine which requires a goal for each specified ray. It is easily employed to adjust the geometric centers along the optic axis; however, there is no auto-collimating feature to adjust optics to produce parallel rays. An important requirement of the spectrometer modeling was to adjust the collimating mirrors to produce collimated beams incident on the gratings. Next, the focusing mirrors were adjusted for the sharpest tangential ray focus at the middle slit and at the original exit slit. This was done because non-imaging spectrometers are aligned for highest spectral resolution, or in other words, sharpest tangential focus. The smallest diameter possible was nine microns at the middle slit and 20 microns at the exit slit. This was found by using the random ray generator feature of the program which essentially fills the optics with randomly angled rays. After all positions and angles were adjusted, the randomly generated rays form a definitive spot where the vast majority of rays converge. Then the flip mirror was added to the system model and the focal planes due to the astigmatism were found. The tangential focus occurred at 209.8 mm from the flip mirror and the sagittal focus occurred at 219 mm from the flip mirror. Finally, the cylindrical lens was included and its position and rotation and the location of the detector focal plane were adjusted simultaneously to produce the sharpest focus of all rays. Using the random ray generator feature, the final spot size at the detector plane was found to be approximately 20 microns by 20 microns. The spot size agrees well with the spectral and spatial observations of Yaney and Blackshire.[12] Figure 13 illustrates the final spot pattern of a few hundred rays generated with the random ray generator. Each point represents a final ray position on the detector plane as traced through the system. The initial position of each ray is at the center of the entrance slit and the angle is randomly generated by the program.

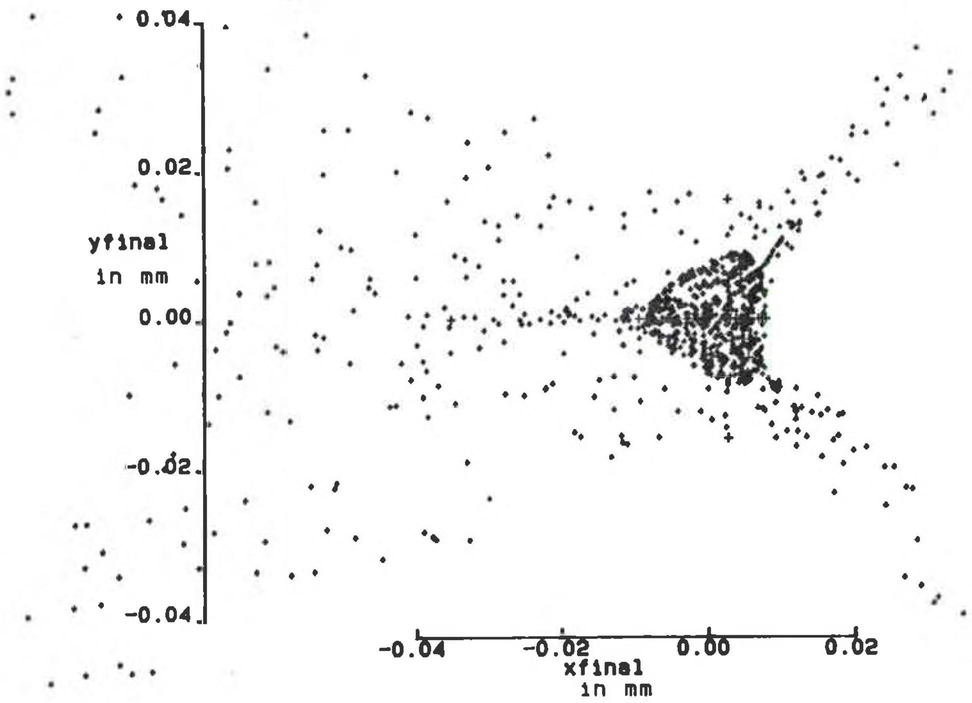

Figure 13: Spot diagram of the image at the detector plane generated by the ray trace program.

Also, because the program is not limited by physical constraints, namely the small distance between the spectrometer wall and the detector, different focal length cylindrical lenses were modeled with the program. Each produced similar final spot patterns and sizes except for 50 mm or smaller focal length lenses. These produced larger spot sizes presumably because of other aberrations associated with high power (short focal length) lenses.

Holographic Edge Filter

The accurate measurement of low-light level Raman spectra requires adequate signal with minimum noise. There are many components and schemes which determine the optical efficiency of the microprobe. There are also many advantages to an increased efficiency. Most notable is that the exposure time can be decreased. This lowers the cosmic ray contaminations of the spectra. A decrease in exposure time also lowers the possibility of accidental movement of the loading jig, the specimen, or the microscope stage which may result in an altered applied stress, a different probe area, or a defocused beam, respectively. Also, the laser probe beam power can be decreased. This reduces the risk of damaging the specimen, which can occur at high laser powers or while the beam is being focused. This section details the modification of the microprobe with a holographic edge filter to reject light at 532 nm.

The intended design of the double spectrometer is to reject all but a narrow range of wavelengths of light from the first half passing through to the second half by using a narrow middle slit. However, imaging spectroscopy using array detection requires the middle slit to be opened to its maximum extent, which does not reject stray light from passing through to the second half of the spectrometer. The resultant spectra contain noise and high background light levels due to the relatively intense reflected and Rayleigh light at 532 nm which can overwhelm the Raman spectrum. For this reason a sharp holographic edge filter manufactured to reject light at 532 nm was chosen to replace the colored glass filter. Other filter designs have drawbacks which holographic filters do not. Dielectric thin film interference filters contain ripples in the transmitted region,[48] colloidal diffraction filters are relatively expensive and colored glass filters have comparatively gradual transmission slopes. The spectral characteristics of the colored glass filter are poor for Raman detection. At 864 cm^{-1} the transmission is only 40%. The effective corner frequency of the glass filter is ~700 cm^{-1}, which restricts detection of Raman modes below this value. It is not possible to choose a glass filter with a corner frequency closer to 532 nm (0 cm^{-1}) because the transmission slope is too gradual in order to reject enough of the intense light at 532 nm.

Recent developments in the processing technology of high quality holographic optical elements solves the problem.[49] The advantages of using a holographic edge filter are a high optical density at the rejected wavelength, steep transmission curve slope, no side bands, and it is tunable. A comparison of the transmission curves of the colored glass filter used here and the recently acquired holographic edge filter are shown in Figure 14. The frequencies of some of the Raman lines of Si_3N_4 are highlighted. Not shown in these curves is the optical density which defines the ability of the filter to reject the intense laser light reflected from the specimen. The holographic filter has a specified density greater than 4.5 at 532 nm.

The design follows that of a notch filter; however, these filters are uniquely designed so that one side of the notch is favored for maximum slope. The other side has poorer slope characteristics. Part of the unfavored slope (the anti-Stokes side) of the notch can be seen in Figure 15. The holographic filter is a Lippmann volume hologram made of 30 microns thick dichromated gelatin sandwiched between two thin plates of glass.[49] The dichromated gelatin emulsion contains volume fringes or layers parallel to the surface of the emulsion.

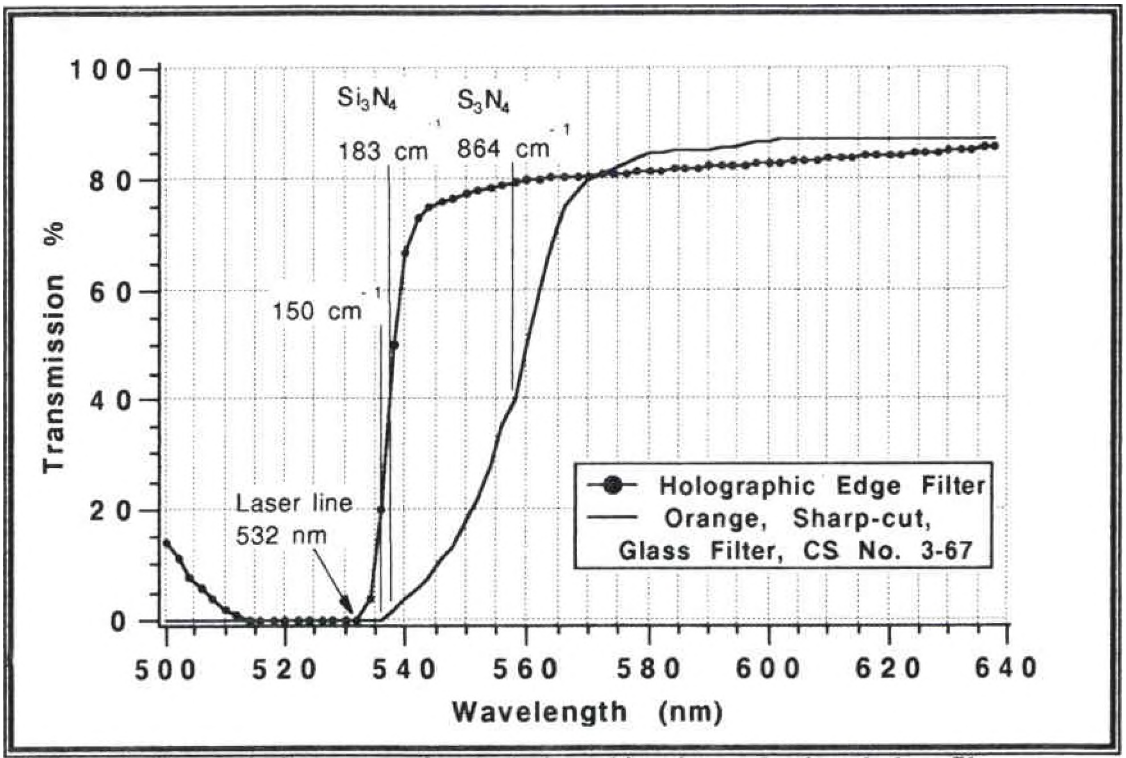

Figure 14: Transmission curves for the holograhic edge and colored glass filters. The positions of some Raman modes of Si_3N_4 are shown. (Taken from References 50 and 51).

The fringes are generated by counter-propagating monochromatic beams which create a standing wave pattern. The pattern is recorded by the emulsion as a sinusoidally varying refractive index n. The fringe spacing Λ is defined by the recording wavelength λ_r given as

$$\Lambda = \lambda_r / 2n \ . \tag{27}$$

The fringes effectively form a half-wave stack interference filter. Only light incident on the filter satisfying the Bragg condition will be diffracted which is determined by a similar equation written as

$$\lambda_i = 2n \ \Lambda \cos \theta_i \tag{28}$$

where λ_i is the incident wavelength and θ_i is the angle of incidence. The relationship between the rejected wavelength and the wavelength the hologram was recorded at is then

$$\lambda_i = \lambda_r \cos\theta_i \quad . \tag{29}$$

Therefore, by tilting the filter a corresponding angle of incidence $\pm\theta$, effectively tunes the transmission curve, but only to lower wavelengths such that the incident (rejected) wavelength λ_i is always lower than the recorded wavelength λ_r. The filter is uniquely manufactured so that the Stokes-Raman side on the transmission curve has a greater slope. This is accomplished in the post-recording stage of the hologram process with successively increased percentage alcohol baths which tends to warp (shrink) the recorded fringes and produce the desired slope.

Proposed Galvanometer Scanner Modification

The holographic filter modification improves the optical efficiency of the system by rejecting the laser wavelength of light. This section describes the proposed modification of the line-illumination design by eliminating the cylindrical optics in favor of scanning the laser beam across the specimen. With this design it is possible to alleviate two significant constraints associated with the cylindrical optics method so as to increase the optical throughput. The first constraint is the Gaussian intensity profile incident on the specimen. With the scanning design it is possible to achieve a uniform intensity profile. The second constraint is the limited length of the line possible with cylindrical optics because of vignetting by the back aperture of the objective. This section is divided into subsections describing aspects of the scanner design which can alleviate these constraints. Other line illumination options are considered first followed by the optical setup. Next, the two methods used to acquire spectra with the array detector are discussed in order to provide a basis for the advantages gained with the scanner design. The emphasis is on a comparison of the maximum incident intensity, maximum line length, and Raman scattered signal possible with the scanner and cylindrical optics designs. This is followed by the specifications and the proposed operation of the scanner. Finally, some possible problems with the scanner design are discussed.

Other Options

Before choosing the optical scanner as the device to overcome the constraints with the cylindrical optics design, other options were explored. To achieve a uniform intensity profile, a Gaussian compensating plate was considered. It would be placed in front of the cylindrical optics and before the focusing microscope objective. This optic, however, cannot be used because a uniform rectangular intensity profile focused by the objective yields a sinc intensity profile at the focal plane. Therefore, if the intensity profile is to remain unchanged through the optics, then the Gaussian profile must be maintained throughout the system. It was then decided to use the Gaussian profile of the laser beam and scan a line on the specimen. If scanned properly, the average intensity would be uniform across the line and furthermore, the line would be lengthened if the beam is scanned into the microscope objective at sharp angles. Two scanning designs were considered: a galvanometer scanner, and an acousto-optic deflector. The deflector, although capable of fast scan rates, is more complicated and more expensive than a galvanometer scanner. The drive electronics typically consist of a voltage-controlled RF oscillator for the transducer which sets up an acoustic, standing wave pattern in the crystal.[52] Consequently, a galvanometer scanner was chosen as the scanning device.

With this modification, the collection optics and detection of the line image remain unchanged, and the cylindrical-lens-spatial-filter assembly is eliminated. Figure 15 illustrates the optical setup with the scanner and its drive electronics. The raw 1mm

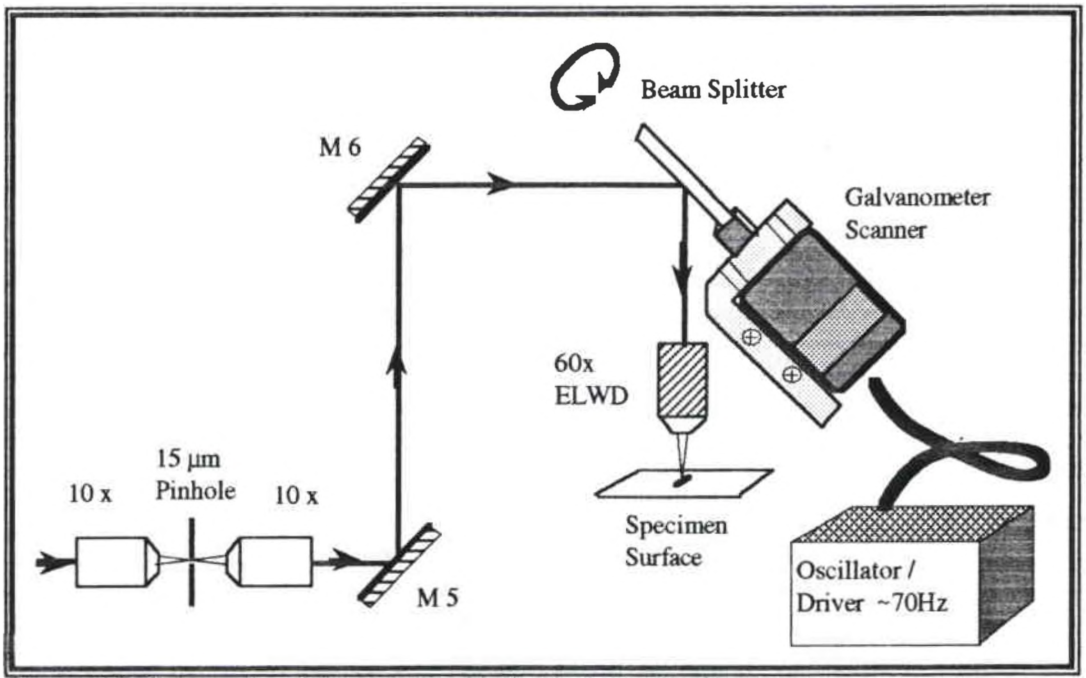

Figure 15: Schematic of the proposed galvanometer design.

diameter laser beam is spatially filtered without magnification using two identical power microscope objectives (10x) aligned opposite to each other and a 15 micron pinhole aperture placed at the common focal plane of the objectives. If the collimating objective is defocused, the beam can be expanded or contracted resulting in a smaller or larger spot size on the specimen surface. Mirrors M5 and M6 are not altered; they direct the beam onto a beamsplitter which is connected to a galvanometer scanner shaft. The repetitive angular movement of the shaft scans a line on the very small 4.9 mm diameter back aperture of the 60x extra-long working-distance-microscope objective. This, in turn, translates the focused beam across the specimen surface to form a line image. By defocusing the collimating objective and controlling the scanning angle, it is possible to precisely control the entire shape of the line. Because the beamsplitter is the scanning optic, its alignment with respect to the beam is not typical of scanning applications. Usually, the scanning optic deflects the beam in the same plane as the incident beam. The direction of rotation of the beamsplitter deflects the beam into a plane perpendicular to the incident beam. The consequence of this is considered in the last subsection.

Acquisition Methods

As discussed previously in this chapter, the array detector allows for resolution of the entire line image on the specimen surface. There are two general methods used to acquire data. The first is to bin pixels in columns via software commands in order to collect all the scattered light along the line. This is used for cases when there is no need to spatially resolve the line image. Not binning any pixels is the second method and is used for studies which require maximum spatial resolution.

With the cylindrical optics design, the expanded Gaussian intensity profile of the beam is maintained throughout the illumination path resulting in a line on the specimen where the ends of the line are significantly less intense than the center. In most data acquisition cases the laser power is adjusted so that the intensity at the center, the most intense part of the line, is just below the damage threshold for the specimen. Therefore, there is less than maximum scattering from regions other than at the center of the line. For the first method of acquisition, the exposure time is determined by the total Raman scattered light along the line. For the second method, the exposure time is determined by the regions on the line with weakest illumination which are the end pixels. The acquired spectra at the ends have lower signal-to-noise ratio since the scattered intensity is less compared to the spectra acquired near the center of the line.

Both methods of acquisition benefit from the scanning design because the intensity profile, when averaged over time, is essentially an ideal rectangular profile. However, this view does not consider the initial reason for using cylindrical optics, which is to spread out the probe beam to reduce specimen heating. If a cw laser is used, then the beam is scanned across the surface with the same power delivered to all segments of the scanned line. In our case, a pulsed laser operating in burst mode only delivers bursts at intervals across the scanned line. Therefore, successive scans are necessary to scan a line of uniform intensity. With the scanner design the unexpanded beam is pulsed at a single one or two micron location. This may damage the specimen if the same power level is used as with the cylindrical optics design since the total power of the beam is focused at a one or two micron spot. If this is true, then the incident power level must be decreased which corresponds to a decrease in the Raman scattering power. Conversely, if the power of a single pulse does not damage the specimen, which is quite possible since the spot size can be expanded a little, then the incident power can be increased with a corresponding increase in the Raman signal. This all depends on the time between pulses at the same probe location and the thermal diffusivity of the material. If the relative decay rate of heat is fast, then the incident power level can be increased. If the decay rate is slow, then the same situation for both designs (cylindrical lens expansion and scanning) exists and the incident power must be slowly increased to allow the material to thermally diffuse the accumulated heat from multiple laser pulses. In this case the total Raman scattered power is greater for a given exposure time because of the uniform intensity profile. Also, there is a loss of power (light), for the cylindrical optics design, in the wings of the Gaussian profile because the expanded line is vignetted at the back aperture of the microscope objective. With the scanner design there is no expansion, or very little expansion, of the beam before the back aperture of the objective.

Because the change in illumination intensity is material dependent and, therefore unknown, the advantage of an increased line length for no change in the intensity only benefits the second method of acquisition. However, a longer line on the specimen, compared to the cylindrical optics design, offers the possibility of observing a larger area on the specimen surface during a single run. This could reduce the total number of exposures to map a structure. The length of the line increases with the scanning design because rotation of the beamsplitter directs the light at relatively sharp angles into the back aperture. Because of the transforming property of lenses, and microscope objectives, the beam translates across the surface of the specimen which lies at the focal plane of the objective. The sharper the angle into the objective, the greater distance from the optic axis the beam translates. Therefore, the closest optic to the objective should be the scanning optic. This is the reason that the beamsplitter was chosen as the scanning optic instead of one of the mirrors as is usual for scanning applications. Ultimately, the scanning angle depends on the distance from the beamsplitter to the back aperture of the objective and the desired length of the line on the specimen surface. The maximum angles and line lengths possible are compared in Table 1 for a distance of 120mm. These were determined by visually observing, through the binoculars, the distance the scanned spot traversed on the specimen surface.

Table 1: Comparison of illumination line lengths.

	Maximum Scanner Angle	**Maximum Line Length**
Cylindrical Lens Design	----------	28 µm
Scanning Optic, Mirror M6	± 0.252°	44 µm
Scanning Optic, Beamsplitter	± 0.358°	100 µm

Specifications and Proposed Operation

The scanner to be used is the General Scanning closed loop scanner, model G325DT.[53] This model's specifications meet some of the requirements for scanning small angles. The G325DT can accommodate optics with relatively large inertia while maintaining a low wobble of less than 25 microradians, optical. The wobble of the scanner is the cross-axis motion, which if too great, results in a deviated line image. Other smaller models of scanners are designed for very small mirrors with correspondingly small inertias, but since the beamsplitter (2.5 mm diameter proposed) is to be used as the scanning optic, a large model scanner with the capability to accommodate large optics is necessary. However, the large size of the G325DT scanner limits the maximum scan rate possible at 80 Hz sinusoidal. The scanner, if operated in the closed loop mode, is position-controlled by feedback electronics in the driver amplifier which monitors the position of the scanner via a capacitive rotation sensor. However, if the scanner is not operated in the closed loop mode then the position is not monitored and the exact beam position can only be determined by observing the angle of the beam or by the input current. In closed loop mode, the zero drift and temperature of the scanner are maintained to increase the precision of the beam position.[53]

The basic operation of the scanner is to optimize the length of the line and control the effective scanning rate. The scanner is to be driven by a power oscillator operating at ±5 volts, ~70 Hz sinusoidal in sync with the laser flashlamp pulses. Because the flashlamp pulses at ~60 Hz, the line effectively scans at a beat frequency of 10 Hz. The timing diagram of the flashlamp pulses with this scanner frequency is shown in Figure 16. During a single flashlamp pulse, the spot is smeared across the specimen. With the operating frequencies given above, a two micron spot is smeared during the 120 microsecond flashlamp pulse to ~2.12 microns. Also, for a flashlamp frequency of 60 Hz, the pulses overlap and the same positions (every 33 1/3 microns) on the specimen are pulsed. Therefore, the effective probed length in a single pass (only three pulses define the line before the same areas are probed again) is only 6.36 microns. The total line length, however, is 100 microns. This obviously isn't scanning a uniform line. However, if the scanner frequency and maximum angle are fine tuned so that the probed area for each pass is at an adjacent spot along the line, the probed area will not be the same. For example, if the flashlamp and scanner frequencies are 60 Hz and 70.1 Hz respectively, then each pulse occurs at every 33 2/3 microns on the specimen so that adjacent probed areas are separated by two microns (the spot size). In ~50 flashlamp pulses the entire 100 micron line is scanned uniformly. This takes 0.833 seconds for a beat frequency of 0.6 Hz. Consequently, the scanner frequency is of utmost importance to maintain a uniform intensity profile.

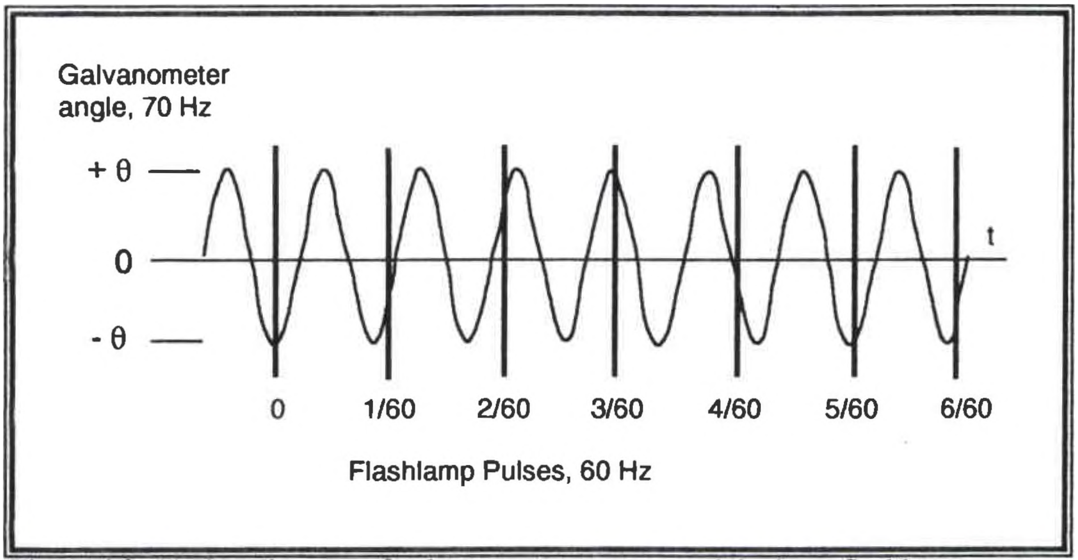

Figure 16: Timing diagram of galvanometer scanner and the laser flashlamp. The pulses mark the scanner angle and position of the beamsplitter.

Possible Problems

The use of the beamsplitter as the scanning optic and the small angles scanned make this design unusual and problematic. Some problems expected include: 1) the field curvature of the objective and the effect on the line image length; 2) the cross-axis wobble of the galvanometer scanner and; 3) the atypical alignment of the scanner with respect to the optic axis.

As stated before, the advantage of employing sharp angles into the back aperture is to maximize the line length. However, at the sharpest angles the beam can be aberrated due to field curvature of the microscope objective and essentially the ends of the scanned line will be less focused than at the center. This corresponds to an increase in the width of the line at locations away from the center position. The scattered signal is not expected to decrease if the scanned line is short enough to avoid field curvature and the entrance slit width is sufficient. The maximum line length with some field curvature is 100 microns and possibly 80 microns for a line with no visually detectable field curvature.

The galvanometer scanner motor is a rotary servo, single-pole motor. As such its precision for a given voltage and current is determined partly by the quality of the bearings. The cross-axis motion, or wobble, of the shaft is a direct result of the roundness of the bearings and is rated at less than 12.5 microradians, peak-to-peak, mechanical (model G325DT).[53] This can be used to find the cross-axis deviation on the surface of the specimen by multiplying the wobble angle by the ratio of visually-determined maximum translation of the beam (50 microns) to the maximum angle (0.358°). This is valid if the microscope objective can be considered diffraction-limited in which case there is a linear relationship between the incident angle and the beam translation at the focal plane. Since the objective is a high-contrast, flatfield achromat, it is assumed to be well-corrected for aberrations. The result is a deviation from the line image on the specimen surface of less than 0.1 micron peak-to-peak. Long-term scanning at small angles has the potential to wear flat spots in the bearings, which would increase the wobble. Occasional full-angle scanning redistributes the oil in the bearings and is, therefore, necessary to alleviate this potential problem.[54]

Because the axis of rotation of the scanner shaft is 45° to the optic axis, the position of the beamsplitter with respect to the beam direction results in a parabolic-shaped image as shown in Figure 17. At large scanning angles, the deviation from a straight line can be significant and, therefore, the entire line cannot be imaged onto the entrance slit of the spectrometer.

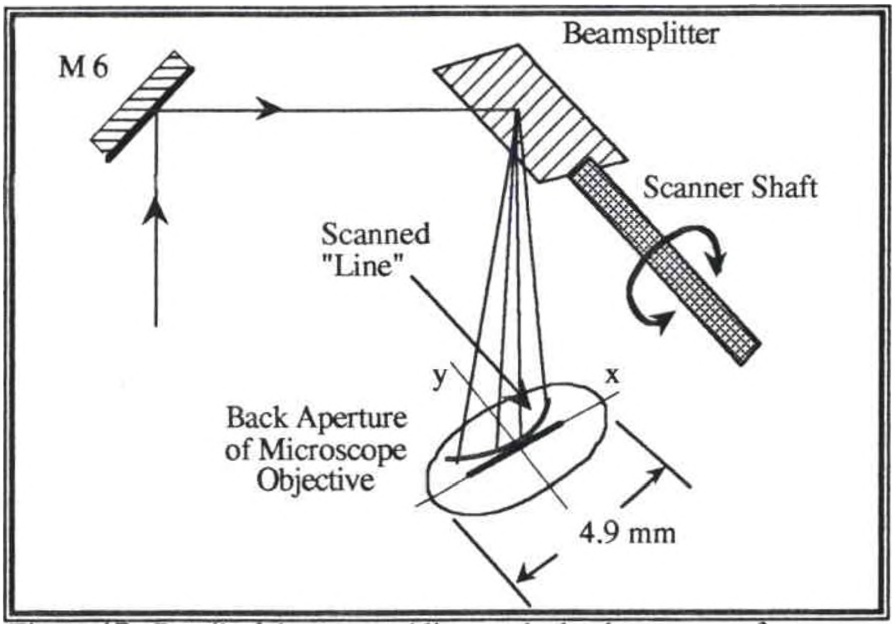

Figure 17: Detail of the scanned line on the back aperture of the objective.

The shape of the line on the back aperture is illustrated in Figure 17 and is written as

$$y = \frac{x^2}{2\,d} \tag{30}$$

where x is the axis of the ideal line, y is the axis of deviation from the line, and d is the distance from the beamsplitter to the back aperture. However, as before, because of the very small scanning angles, the deviation in the y-direction is minimal and does not limit the effective line length. The coordinates of the deviated beam at its maximum position on the back aperture of the of the objective are (± 1.0604, +0.0047) mm for a scanning angle of ±0.358°. In the y-direction the angle of the beam into the microscope objective is 39.16 microradians and, under the same imaging assumptions used to calculate the wobble deviation on the specimen surface, the maximum coordinates of the line image are then (±50.0 , 0.3134) microns. Since the spot size is typically two microns on the surface, the deviation of 0.3 microns is not expected to be significant.

CHAPTER IV

EXPERIMENTS

The Raman spectra of Norton/TRW NT-154 β-Si_3N_4, specimen numbers 54, 55, and 58 were measured for the experiments discussed in this chapter. Initially, the intensities of the 864 cm^{-1} mode and the lattice modes of β-Si_3N_4 were studied to demonstrate the advantages of using a holographic edge filter. The main thrust of the thesis, however, was to record the shift of the 864 cm^{-1} mode due to stress fields produced in two different loading conditions. The first loading study was to map the stress gradient across a specimen under flexural stress and the second loading study was to map the stress field at the tip of a crack on the tensile surface of a specimen.

Holographic Filter Characterization

As discussed in Chapter III, an adequate filter is necessary for Raman imaging spectroscopy to reduce the high intensity of the laser line passing through the spectrometer. The design of the holographic filter chosen to replace the colored glass filter was discussed in Chapter II and has four main properties: 1) it has a very steep transmission curve slope near the laser wavelength; 2) it exhibits high optical densities in the no-pass region; 3) it has ripple-less transmission; and 4) the transmission curve can be tuned by tilting the filter at some small angle with respect to the incident laser beam.

To investigate the steep slope property, the intensities of the 864 cm^{-1} mode of β-Si_3N_4 were observed for three methods of filtering and illumination and are plotted in Figure 18. The original method involved the use of the colored glass filter and also a

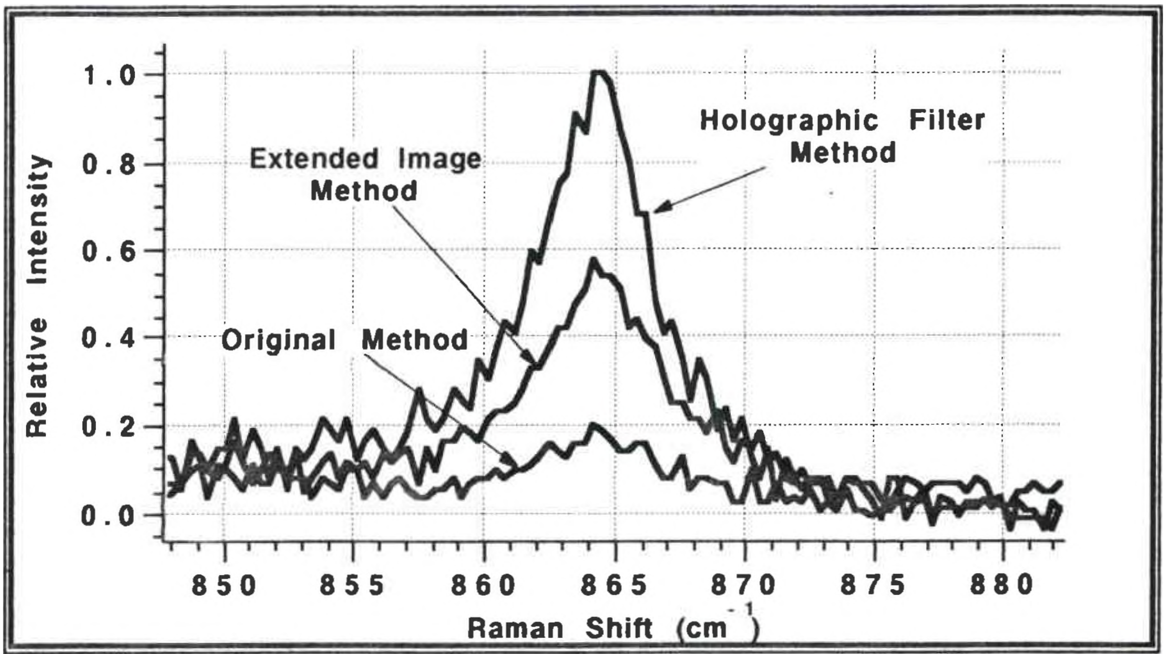

Figure 18: Intensity comparison of three methods of spectra acquisition. The holographic method is a combination of the extended and the use of the holographic filter. The exposure time is 10 minutes.

modest defocus of the first cylindrical lens to produce a line image of laser light on the specimen surface. The intensity profile of this line image is a Gaussian in both dimensions with a maximum intensity at the center of this line and essentially zero intensity at the ends and edges of the line. The majority of runs performed for this work utilized the holographic filter and a more defocussed image which produced a more extended Gaussian profile thereby reducing the possibility of specimen heating at the center position. This allowed the laser power to be increased 25% from 0.76 mW to 0.94 mW average power on the specimen. The contribution of this extended image adjustment without the holographic filter is shown in Figure 18 labeled as the Extended Image Method, and the method of using both is labeled as the Holographic Filter Method. All methods shown have the same operating parameters among which is a 10 minute exposure time. The maximum power at the specimen used for both focussing methods is defined as the power just below that which damages the specimen. The average power used for the majority of the experiments was ~0.75 mW to avoid accidental damage to the specimen. The background levels for the three methods are different but they have been subtracted out in order to compare the peak intensities.

The tilting property of the filter was investigated using the lattice modes of β-Si_3N_4 observed at ~186 cm^{-1}, 206 cm^{-1}, and 224 cm^{-1}, because they are situated near the slope of the transmission curve. The spectra of the lattice modes for three tilt angles are shown in Figure 19.

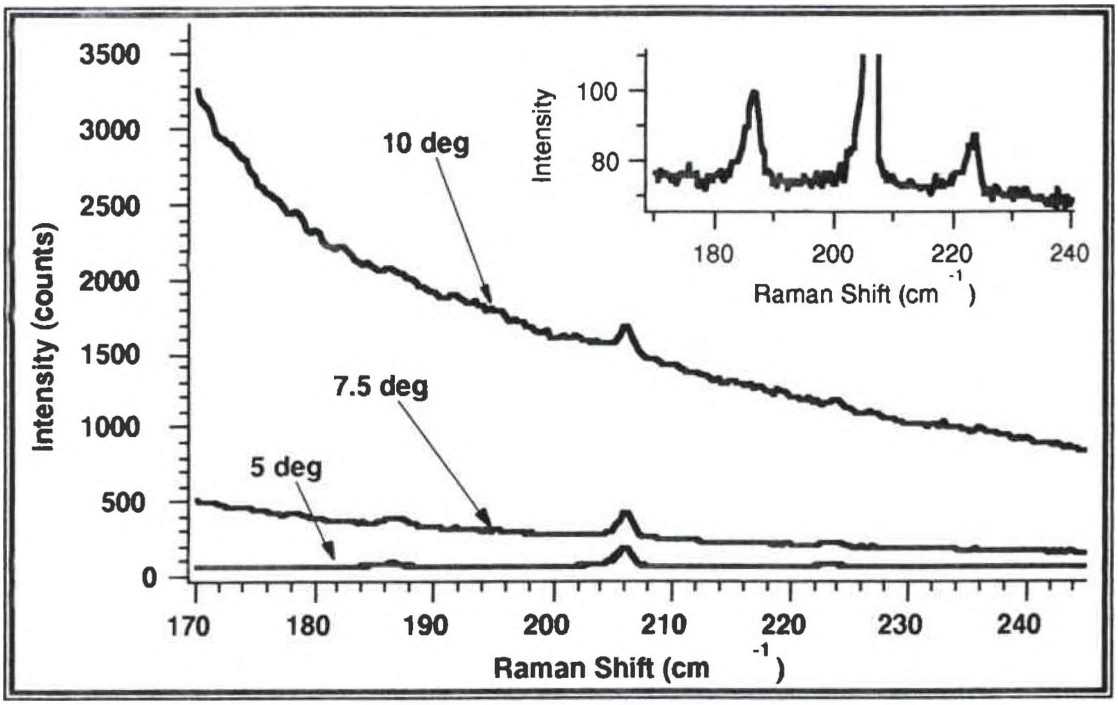

Figure 19: Lattice modes of β-Si_3N_4 at three tilt angles of the holographic filter. The inset is an expanded view of the 5° tilt angle. The exposure time is 3 minutes.

The background level increases dramatically at large tilt angles because of the combined effect of the blooming of the intense laser line at the detector and the translation of the no-pass region of the filter to lower wavelengths away from the laser wavelength (zero wavenumbers). No change was observed for tilt angles up to 5 degrees.

Strain-Induced Mode Shift

For all strain-induced mode shift measurements, the mode shift was determined by subtracting the 864 cm^{-1} peak spectral position from the 915 cm^{-1} nitromethane reference peak. The peak positions were determined by fitting the Lorentzian function to the recorded Raman lineshape. A typical fit to an 864 cm^{-1} mode is shown in Figure 20. The Lorentzian fit is a result of a simultaneous fitting of the height, width, position and background level using the chi-squared minimization method. This procedure was performed by the Igor plotting program on a Macintosh IIsi computer. The standard deviation of the peak position fit is shown. The reference Raman mode is generated by a cuvette of nitromethane located at a focal plane in the collection optics before the spectrometer and is, therefore, radiated solely by the reflected light from the specimen.

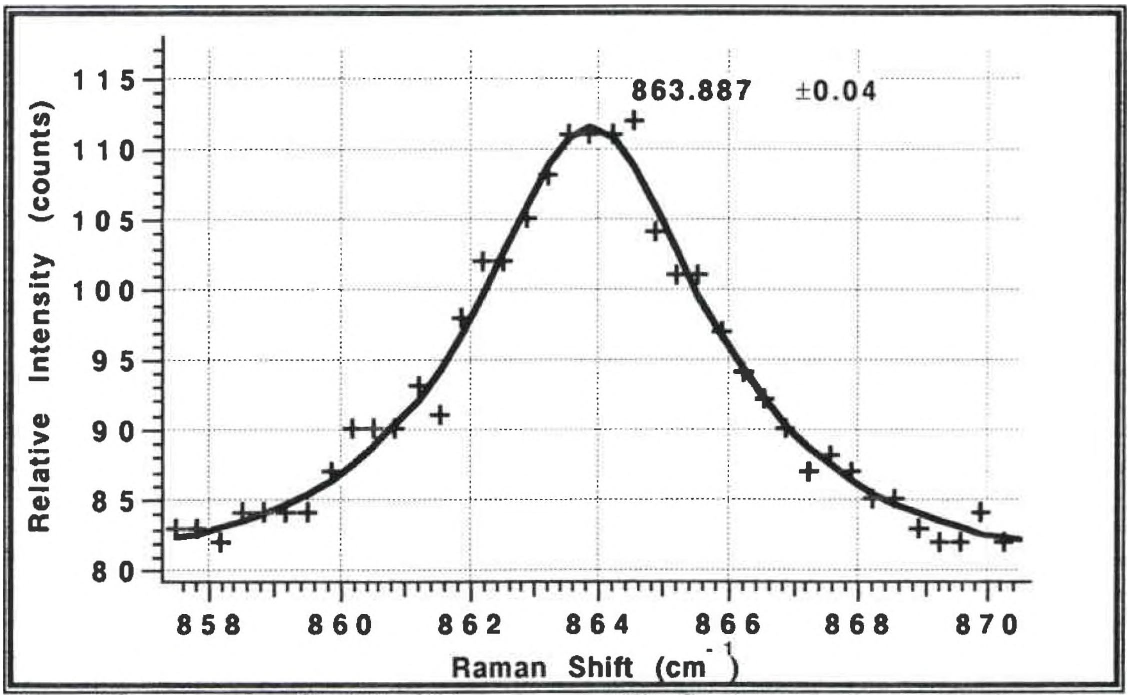

Figure 20: Lorentzian fit of the 864 cm^{-1} mode. The fit gives a peak wavenumber position and a standard deviation to the peak value.

Two spectra containing the reference mode (915 cm^{-1}) and two Si_3N_4 modes (864 cm^{-1} and 922 cm^{-1}) are shown in Figure 21 and are typical of the many spectra used for a strain mapping. Each spectrum has its own Si_3N_4 (864 cm^{-1}) and reference mode positions as

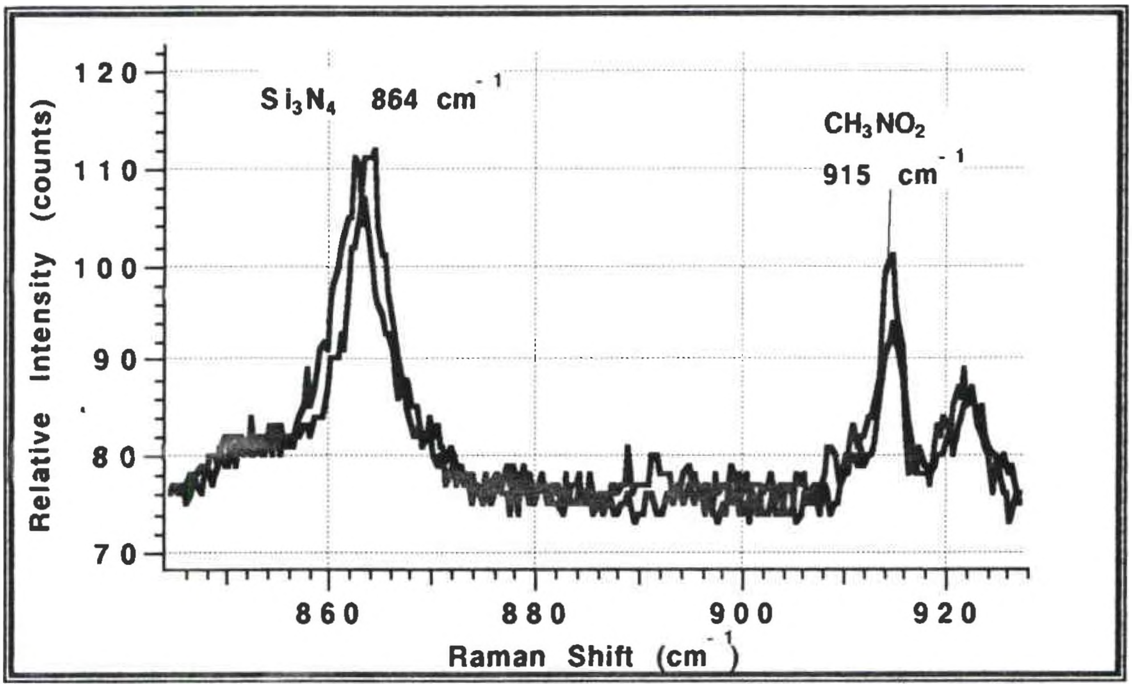

Figure 21: Two typical spectra of stressed and unstressed Si_3N_4 and reference Raman modes. Note the 864 cm^{-1} modes are shifted slightly due to stress while the reference modes have the same peak position.

as determined by the Lorentzian fits. Subtracting these values provides a precise measure of the relative position of the 864 cm^{-1} peak independent of the calibration of the spectrometer and the actual value of the laser wavelength. A control run consisting of 14 simultaneous spectra was performed to determine the mean difference shift between the 864 cm^{-1} β-Si_3N_4 and the 915 cm^{-1} nitromethane at no load. Every difference shift due to stress was then subtracted from this number (50.9135 cm^{-1}) to obtain a precise Raman shift of the 864 cm^{-1} mode with respect to the 915 cm^{-1} mode. Therefore, the shifts of all spectra are accounted for and compared to a single control value maintaining self-consistency between spectra. The control run data is shown in Figure 22.

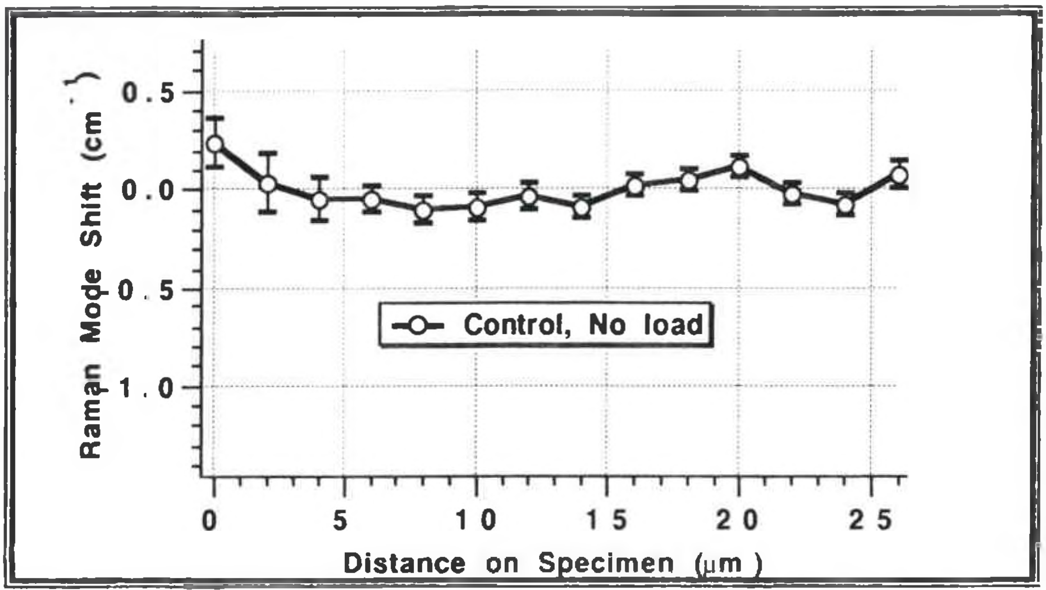

Figure 22 : Control run of Raman mode shifts under no load conditions on specimen #54.

The parameters for this run are similar for all the runs performed to study the crack tip stress distribution. The tension-to-compression study runs used the binning method of acquisition in which the entire illumination line is added together at the array detector creating a single spectra. The line length on the specimen was 28 microns and this usually corresponded to 14 stripes on the array detector representing 14 distinct spectra for each probe location. For the crack tip studies, the intensity of the line image is Gaussian and is weakest at the ends. Therefore, only spectra with a signal-to-noise ratio of greater than 5 were used which was usually 14 spectra. The standard deviation of the Lorentzian fit of each spectrum is shown in Figure 22 and is typically ± 0.07 cm^{-1}. The deviation of the Raman mode shifts should ideally be zero since there is no applied stress. However, the standard deviation of the 14 values is ± 0.09 cm^{-1} which suggests that either 1) the crystallites in their natural states exhibit small amounts of strain or 2) there was some small experimental error in this procedure, or 3) both circumstances were present. A total exposure time of three hours was required to obtain an adequate signal-to-noise ratio in the spectra. Furthermore, because each spectrum represents one horizontal stripe of pixels on the detector, as opposed to 40 stripes binned together, cosmic ray contamination was not prevalent. An overview of the test sequences performed is given in Table 2.

Table 2: Parameters of the test sequences performed.

Tension-to-Compression Study

- Probe located on the side of specimen.
- Binning method of acquisition.

Run #	Specimen #	Filter Type	Exposure Time per Spectrum	Load
Run A	NT-154 #58	Colored Glass	90 minutes	80 lb
Run B	NT-154 #55	Holographic Edge	20 minutes	100 lb

Crack Tip Study

- Probe located on tensile surface of specimen in front of the crack tip except for Run IIb which was located 10 μm in front of the crack tip.
- No binning used. All detector stripes resolved.
- Three hour exposure time.
- Specimen NT-154 # 54.

Run #	Crack System	Load
Ia	Crack due to indent	0 lb
Ib	“	10 lb
Ic	“	0 lb
IIa	After crack propagated due to a 20 lb load applied then released.	14 lb
IIb	Crack arrested after load released.	14 lb
IIc	“	0 lb

Tension-to-Compression Study

As described in Chapter II, a bar bent in a four point bend fixture has both a tensile and compressive face. To measure the strain gradient of the bar on its side, the probe beam was positioned as shown in Figure 23.

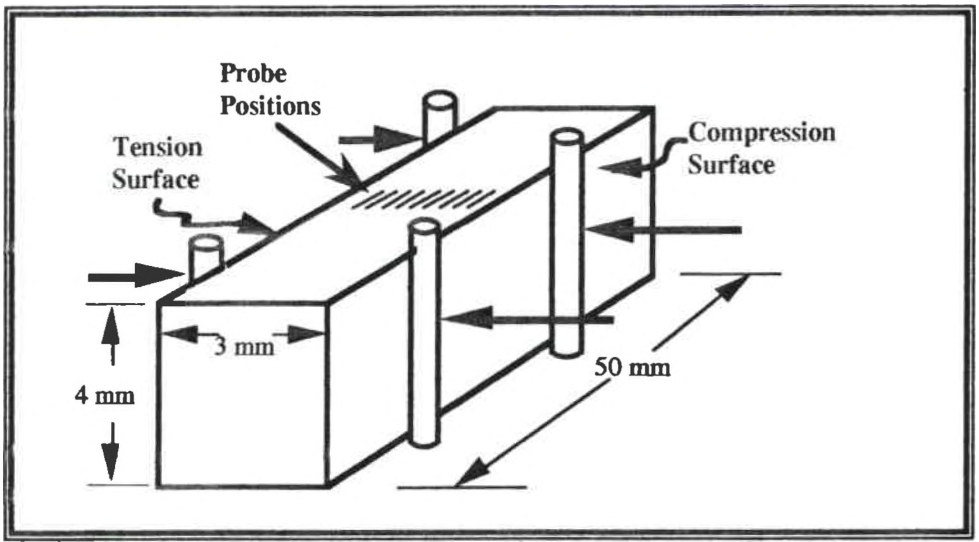

Figure 23: Probe positions on the side of the specimen in flexure.

The probe line was situated in a uniform stress field, perpendicular to the tension and compression surfaces, so that the scattered light from the entire line could be binned together to form one spectrum. Two separate runs were performed on two specimens of β-Si_3N_4. Run A used a sharp cut-off, colored glass filter and required an exposure time of 90 minutes while a holographic edge filter was used for Run B which resulted in an exposure time of 20 minutes for each probe location. In each case 40 pixel stripes were binned although most of the Raman signal was from the center 14 stripes. Therefore, the resultant probe length was ~28 microns. The Raman shifts of the 864 cm^{-1} mode at each probe position are shown in Figure 24 and 25 for the two runs.

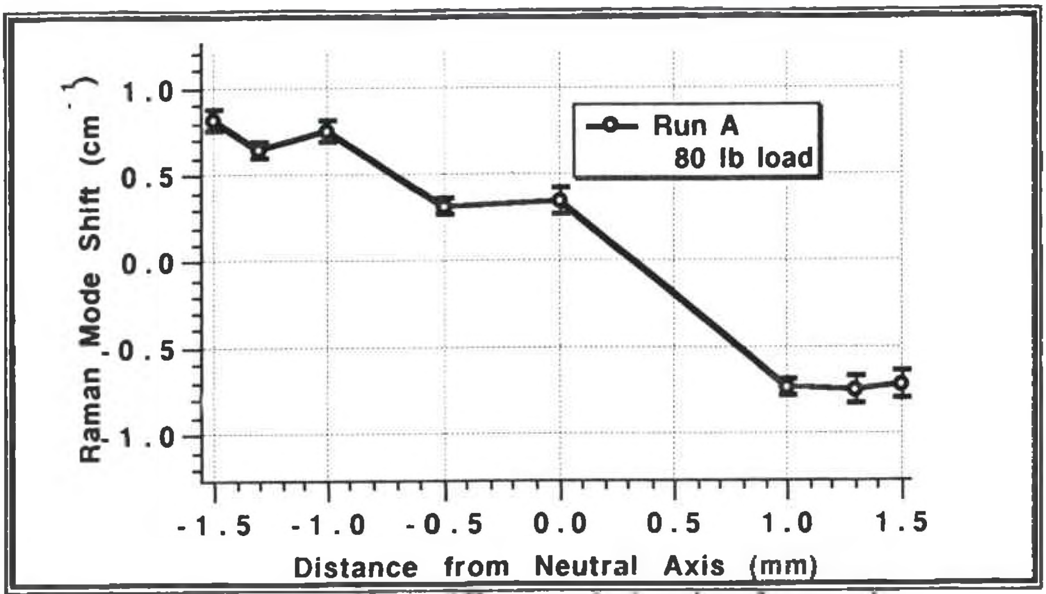

Figure 24: Raman mode shifts at different probe locations from tension (left) to compression (right).

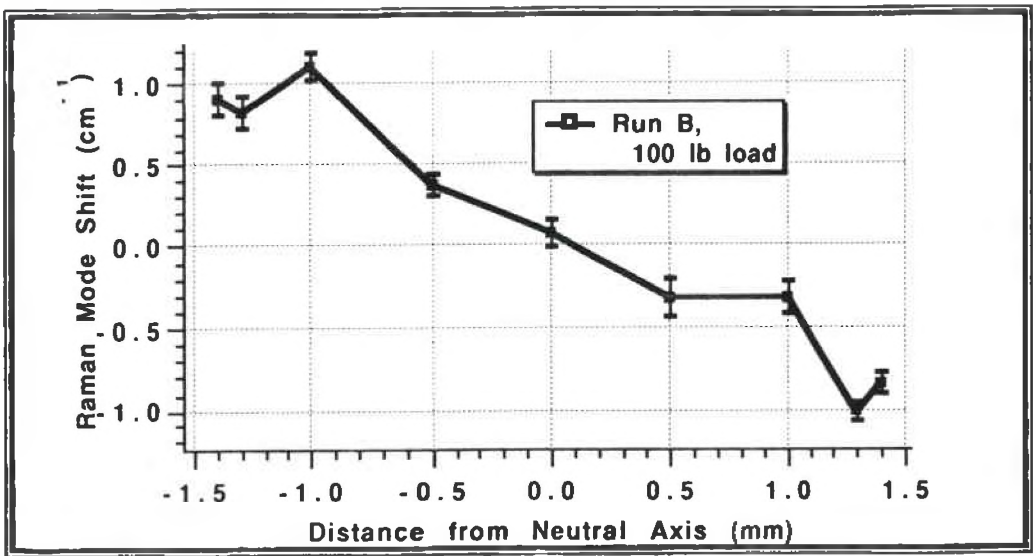

Figure 25: Raman mode shifts at different locations from tension (left) to compression (right).

The horizontal axis designates the probe location along the side of the bar from the compression edge (-1.5 mm) to the tension edge (+1.5 mm). The neutral axis of the specimen is at 0 mm. The resultant standard deviations from the Lorentzian fits of both Raman modes, 864 cm^{-1} and 915 cm^{-1} were calculated using quadratic error propagation and are shown as error bars in the plots.

Crack Tip Studies

A series of runs were performed at the tip of a crack on the tensile face of specimen number 54. The crack was formed with a Vickers diamond indent at 7 kg loading. The indent lies in the center of the bar on the 4 mm-wide, polished tensile face. Only this face of the specimen was polished so that the cracks could be seen and accurately measured under a microscope. The specimen was polished on a Struers Abrapol-2 polisher wheel with successively less course grit and finished with colloidal silica on a medium knapped cloth.

A photo-micrograph of the indent is shown in Figure 26 and a magnified photo-micrograph of the crack tip is shown in Figure 27. Subsequent loading of the specimen in four-point flexure was carried out with the indent on the tensile surface. The resulting surface tensile stress tends to open the cracks aligned perpendicular to the stress field. The length of the entire flaw from crack tip to crack tip due to the indentation was 209 microns. This study relied on a data acquisition method in which the line illuminating the specimen is spatially resolved. Individual pixels in the spatial dimension on the detector are resolved which corresponds to a two micron spot size on the specimen surface. A spot size of two microns probes 1-2 crystallites depending on the size and orientation of the crystallites and, consequently, the Raman mode shift may fluctuate due to the varying microstress on each crystallite and the orientation of the uniaxial crystallites.

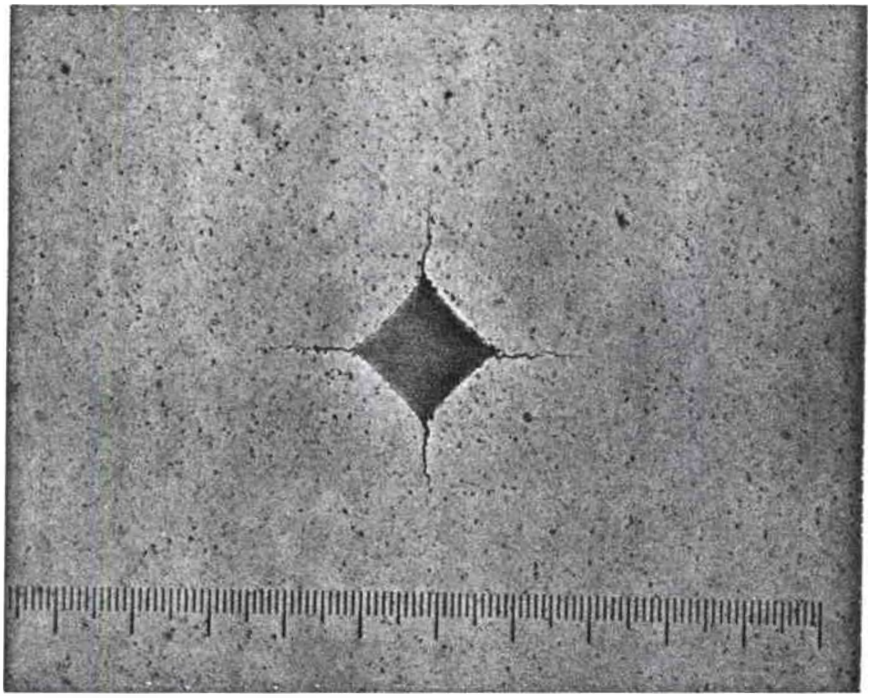

Figure 26: Photo-micrograph of 7 kg indent at 400x. One minor division equals five microns.

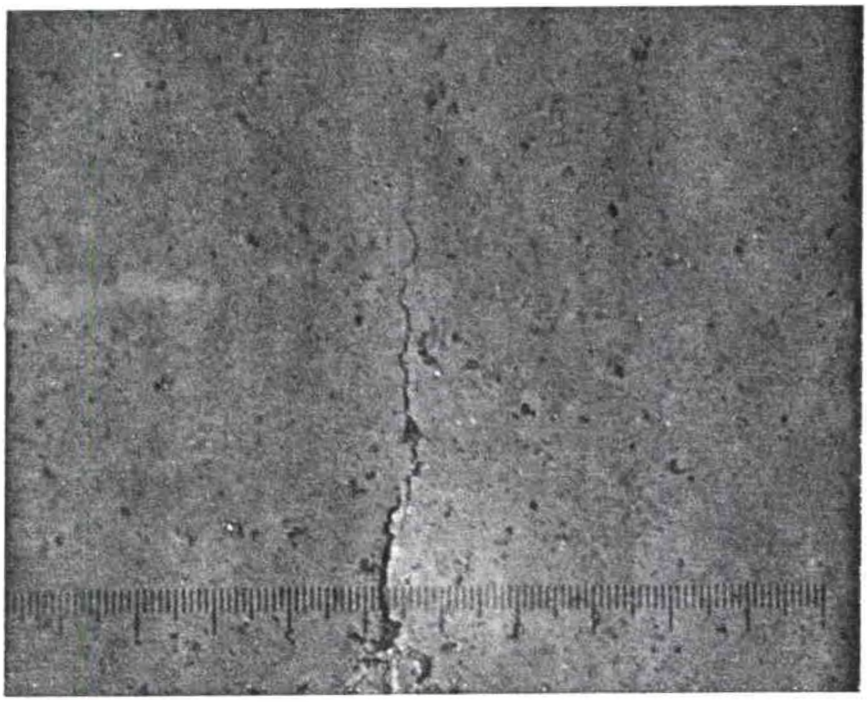

Figure 27: Photo-micrograph of top crack at 1000x. One minor division equals one micron.

The first set of Runs, Ia, Ib, and Ic were performed on the top crack in Figure 26 at the crack tip location formed by the indent. The second set of Runs, IIa, IIb, and IIc were performed after a critical applied stress had propagated the crack to a new physical location. The probe locations of Runs Ia, Ib, and Ic are shown in Figure 28. Run Ia was performed with no applied load and a second run, Ib, was performed with 10 lbs load at the same probe location. This loading corresponds to a surface tensile stress of 59.5 MPa. The third run, Ic, was performed at the same location one week later under no load conditions. No crack growth was observed during or after this loading. The location of the crack tip was determined by visual inspection through the binocular microscope. The probe lines of Runs Ia, Ib and Ic were located in front of the tip of the crack, in line with the extension of the crack, with a few microns of the line overlapping the crack. Therefore, some of the

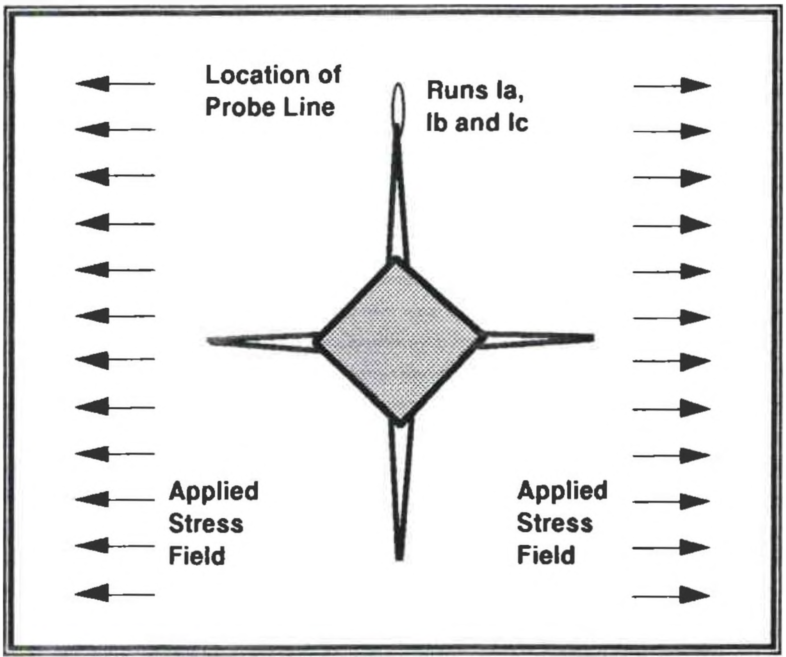

Figure 28. Schematic of indent and positions of probe line for Ru ns Ia, Ib, and Ic.

spectra were obtained at locations where the material had ruptured. The Raman mode shifts from these three runs are shown in Figure 29.

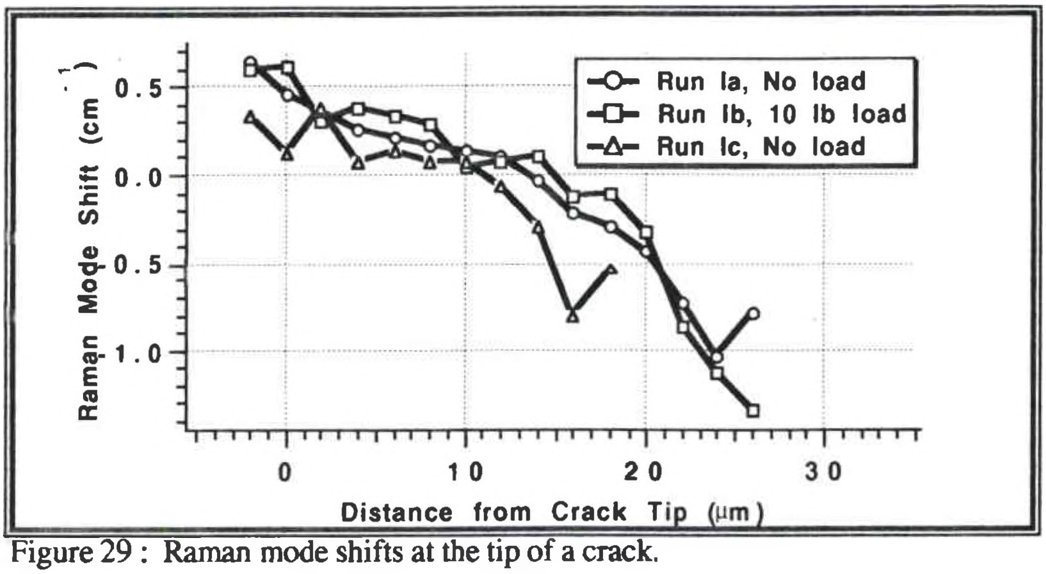

Figure 29 : Raman mode shifts at the tip of a crack.

Because the original intention of the crack studies was to observe a stress intensity due to an applied load, the load was increased to 20 lb (119 MPa. surface tensile stress). Under these loading conditions the crack propagated. To prevent complete fracture, the load was released and only 14 lb (83.3 MPa.) was applied. After 20 minutes the crack had arrested and the new total flaw length increased by 61 microns to 270 microns. Unfortunately, the additional growth could not be seen at the time the specimen was photographed again. Two runs, IIa and IIb, were performed at probe locations approximately illustrated in Figure 30. The data from these two runs are shown in Figure 31.

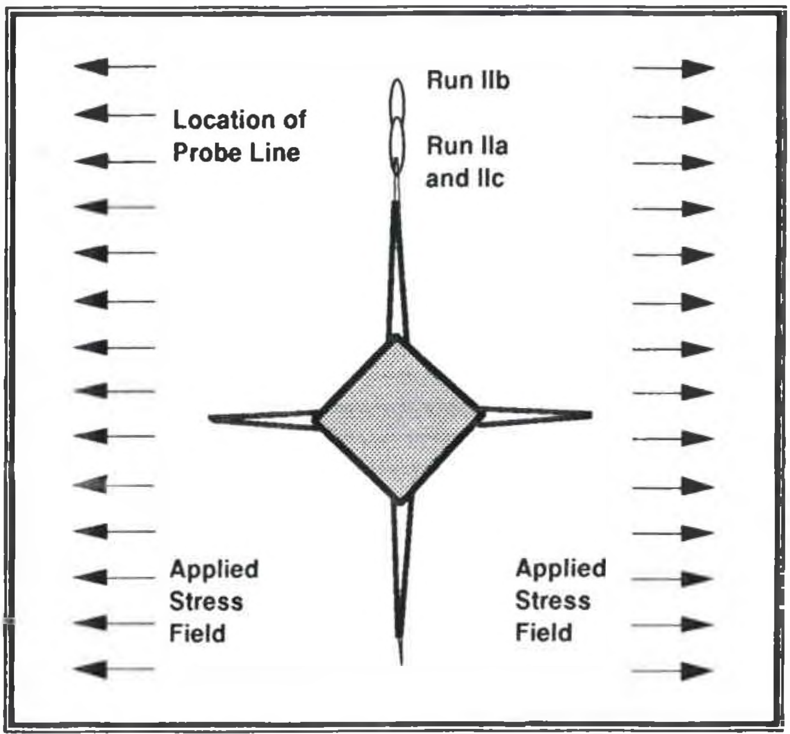

Figure 30: Schematic of indent and positions of probe lines for Runs IIa, IIb and IIc. Runs IIa and IIc are at the same location.

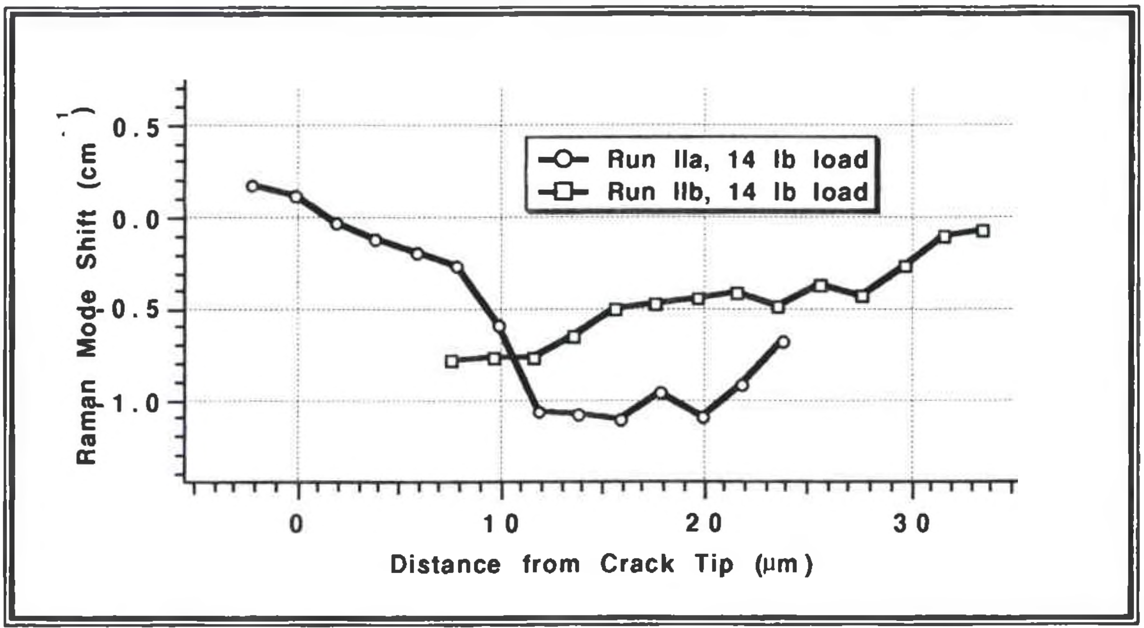

Figure 31: Raman mode shifts for Runs IIa and IIb, corresponding to near the crack tip and displaced from the crack tip, respectively, after the crack had propagated due to a previously applied load.

Another run, IIc, was performed at the position nearest the crack tip just after the 14 lb load was released. The data from these three runs are shown in Figure 32.

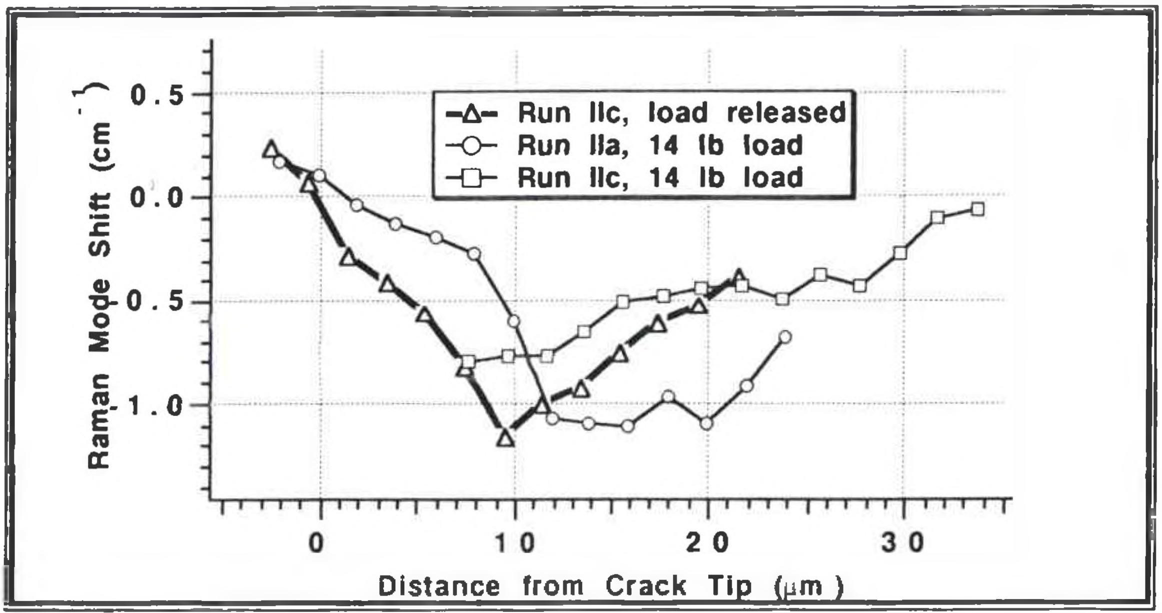

Figure 32: Raman mode shifts for Run IIc, positioned at the crack tip with no applied load.

CHAPTER V

RESULTS AND ANALYSIS

Holographic Filter

The use of the holographic filter significantly increases the optical throughput of the Raman scattered light. Both the use of a more defocussed image and the holographic filter together permitted the study of crack tip strain fields. Each run in which all the pixels on the detector were resolved required a three-hour exposure time. Without these modifications, an exposure time of 13.5 hours would have been necessary for a similar signal-to-noise ratio.

The tunability of the filter is restricted largely by the rise in background intensity as shown in Figure 19 in Chapter IV. With a 10 degree tilt the background overwhelms the 186 cm^{-1} Raman mode whereas with a smaller tilt angle of 7.5 degrees the peak minus background intensity increases slightly. This indicates the slope of the transmission curve at 7.5 degrees is situated such that sufficient laser intensities are blocked and the 186 cm^{-1} mode is passed by the filter with less attenuation than for zero or five degrees tilt. In summary, the performance depends on the intensity and spectral position of the Raman mode to be detected and how well the transmission slope and tilt tuning matches these specifications. The performance at small Raman shifts depends mostly on the steepness of the transmission slope. The majority of the properties of the filter could not be studied without additional equipment. However, based on these studies, the filter performed according to the specifications.

Strain Mapping

In this section, the Raman spectra of Si_3N_4 as presented in Chapter IV are analyzed in order to provide some insight regarding the effect of applied stresses on the 864 cm^{-1} Raman mode. The two experiments performed rely exclusively on the 864 cm^{-1} Raman mode shift which is a consequence of the strain (microstrain) of the Si_3N_4 crystal and not the yttria oxide in the material although it may affect the microstrain in the crystallite. The strain, however, cannot be measured exactly and must be calculated from the bulk Modulus of Elasticity and the applied stress on the specimen. This is inherently ambiguous since the material is polycrystalline, and therefore, the applied stress is not the same as the microstress on the crystallite. Nonetheless, there is a linear relationship between the applied stress and the Raman mode shift found in Si_3N_4[55] as well as other crystalline materials.[56] This relationship can be utilized to plot the data in terms of stress versus distance on the specimen, once a conversion factor has been found, with the understanding that the data (the β-Si_3N_4 Raman mode shifts) are based on the microstrain in the Si_3N_4 crystallites.

The ratio of the applied stress to the 864 cm^{-1} Raman shift is determined using the data from the tension-to-compression study. A straight line fit to the data is shown in Figure 33a and 33b. The fit was adjusted for zero Raman shift at the neutral axis of the specimen and yields a slope in terms of Raman mode shift per distance (cm^{-1} / mm). This is divided into the theoretical value of stress along the side of the specimen, Equation (18) in Chapter II, which is given in terms of stress per distance (MPa / mm). The result is a conversion factor from Raman mode shift to stress. The conversion factor is used to convert the Raman shifts in the crack studies to a stress value so that the crack tip stress field can be interpreted in terms of stress and not simply Raman mode shift.

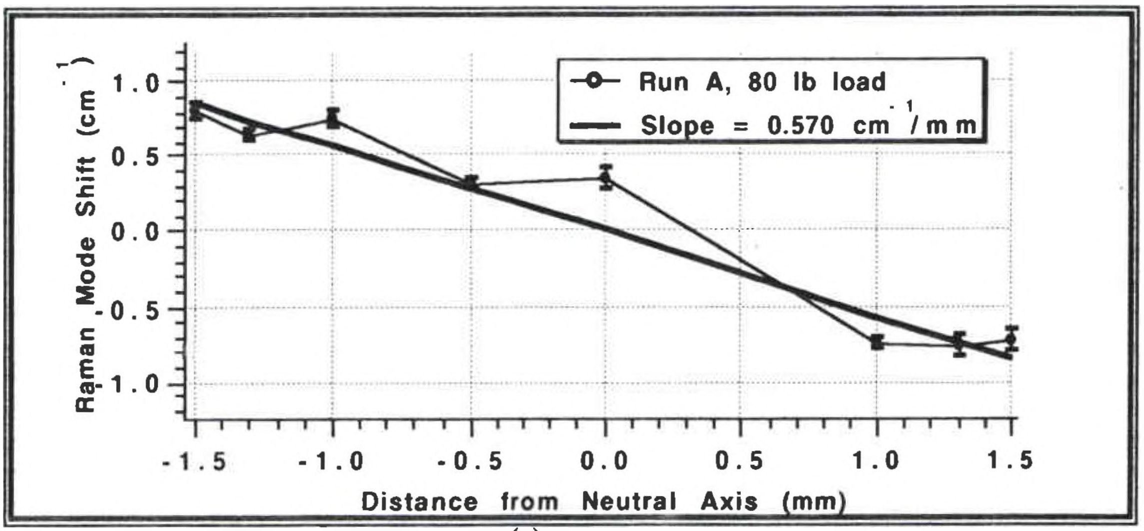

(a)

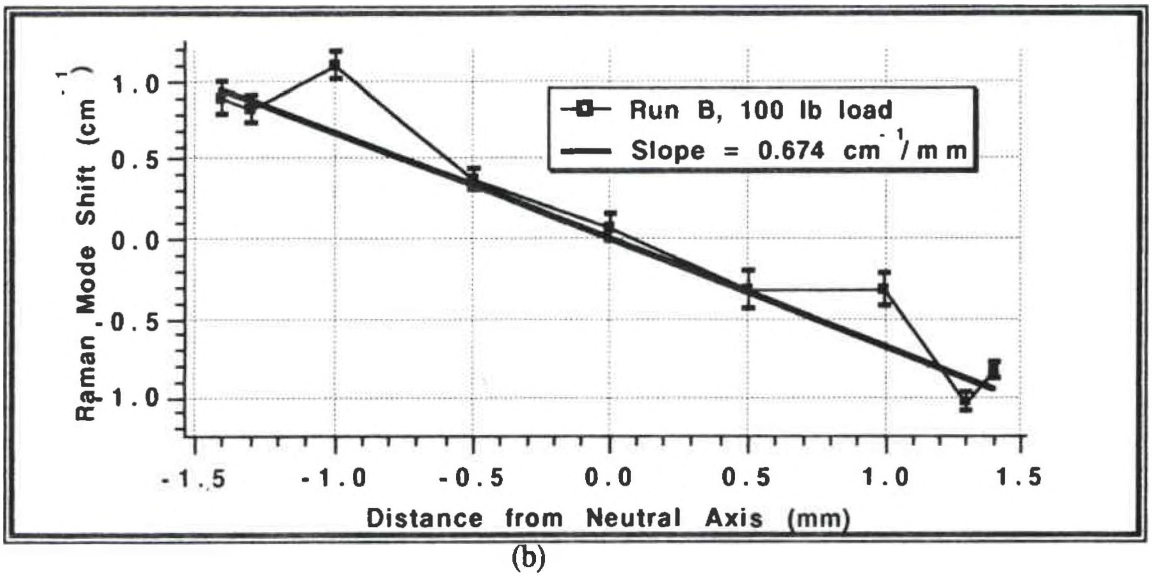

(b)

Figure 33: Line fit to tension-to-compression data for specimens # 58 (a), and # 55 (b). The slope determines a conversion factor from Raman shift to stress.

Tension-to-Compression Study

As discussed in the previous chapter, two runs were performed to determine the strain distribution along the side of a mechanically stressed beam. Using the procedure described above, the stress-to-Raman-mode-shift ratio was computed and the results of the runs are shown in Table 3.

Table 3: Calculated parameters for the tension-to-compression data of two specimens of Si_3N_4 beams.

	Specimen Number	Load (lbs)	Raman Mode Shift Line Fit (cm^{-1} / mm)	Theoretical Stress (MPa / mm)	Stress-to-Raman-Mode-Shift Ratio (MPa / cm^{-1})
Run A	58	80	0.570	195.3	342.6
Run B	55	100	0.674	240.8	357.3
				Average :	349.9

Because the specimens were subjected to different applied bending stresses, the slope and maximum mode shifts are also different. The calculated values of the stress-to-mode-shift ratio, however, agree well with each other as expected. The stress distributions of Runs A and B and the predicted stress distributions according to Equation (18) are plotted in Figures 34 and 35, respectively. Both distributions follow the theoretical stress quite well in the compressive region (Raman up-shifts) and in the tensile region (Raman down-shifts). It is worth noting that the stress-to-Raman-mode-shift ratio is slightly greater than in previous studies on the same material. An average of the mode shifts measured by Blackshire and Yaney[12] reveal a smaller ratio of 279 MPa / cm^{-1} for probe lines located on the tensile surface of a specimen of the same material loaded at 80 lb. The source of the discrepancy is not clear. However, it is possible that there are non-uniform frictional forces at the load points on the flexure jig which could result in a non-uniform load on the specimen.[57]

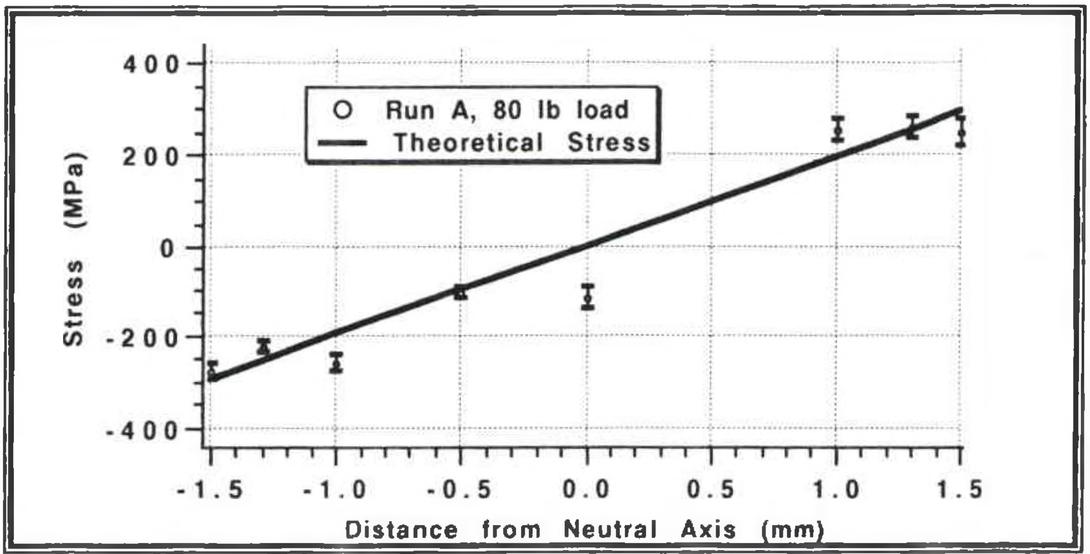

Figure 34: Tension-to-compression stress gradient for Run A, specimen #58.

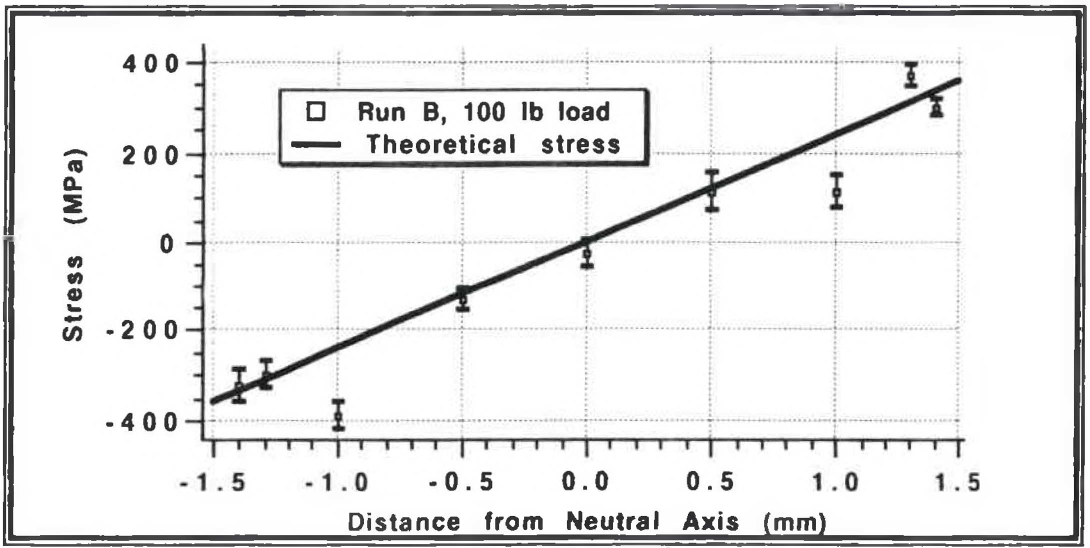

Figure 35: Tension-to-compression stress gradient for Run B, specimen #55.

Strain Field Studies at a Crack Tip

This section is devoted to a discussion of two sets of data for crack tip stress fields. Runs Ia, Ib, and Ic are data for the stress at the tip of a crack made by a diamond indent. The second set, Runs IIa, IIb, and IIc, are stress maps at the tip of a crack that had propagated due to applied tensile stress. As noted before, the Raman mode shifts for the crack tip studies are based on a data acquisition method capable of resolving a two micron spot size. The data for the control run is presented in Figure 23 in Chapter IV and does not indicate any significant variation in microstrain along the length of the probed area.

The results of Runs Ia, Ib, and Ic are shown in Figure 36. The conversion factor from Raman shift to stress used was the average of the strain-induced Raman shift ratio from the tension-to-compression study of the specimen on its side (349.9 MPa / cm^{-1}). The stress field in front of the crack tip does not follow the typical stress field of the K-dominated zone,[43] defined in Equation (21) and shown in Figure 9 in Chapter II. The opposite, increasing tensile stress trend is seen here indicating the region probed was in the process zone.[45] The highest stress value cannot be determined from Runs Ia, Ib or Ic and, therefore, the exact process zone is unknown for these conditions. All three stress distributions show a region of considerable compressive stress behind and in front of the crack tip. The maximum compressive stress lies behind the tip where the ceramic has ruptured. This could be due to bridging or closure stresses which occur behind the crack

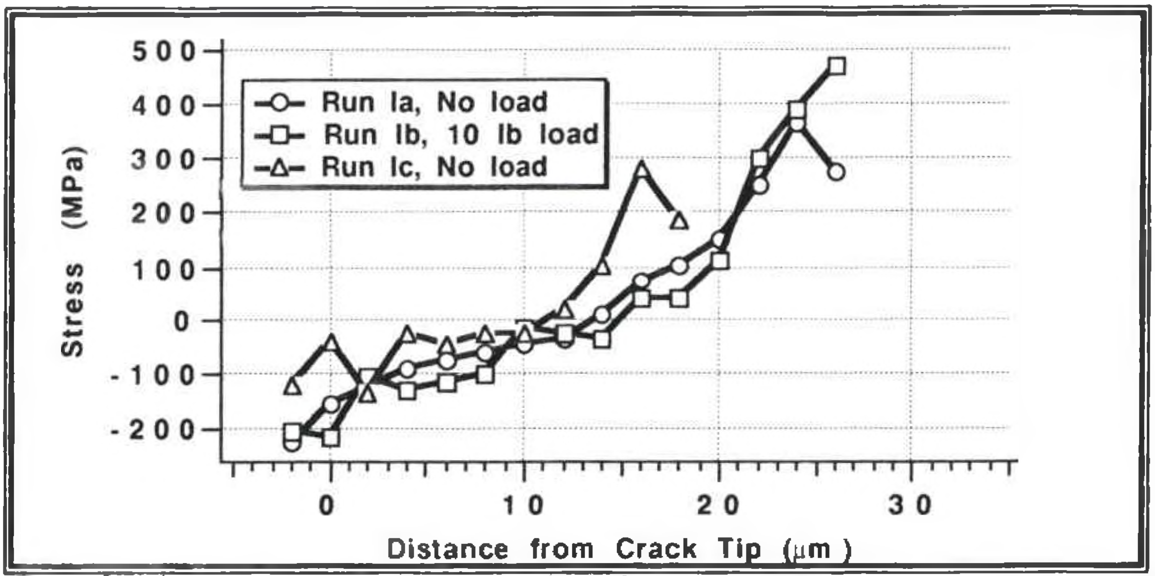

Figure 36: Stress distribution at the crack tip, before propagation.

tip and, therefore, the location of stress reversal, zero stress, may indicate the actual crack tip. This compression region is not predicted with the linear elastic model or with the modification to include a process zone,[45] but is not contrary to those ideas obviously because the theory does not consider stresses behind the tip where the bridging stresses are predominate.[58]

The stress distribution shows that a 10 lb load, equal to 59.5 MPa, is not enough to establish an observable change in the process zone indicative of a larger stress intensity than the original stress intensity due solely to the indentation. Given that Run Ic was taken one week later from Runs Ia and Ib, the study shows 1) excellent repeatability of the data, and 2) the stress field in front of a crack remains unchanged under 10 lb applied load. The equilibrium at the crack tip established by the indentation appears very stable.

With the applied load of 20 lbs, the crack propagated. The load was released and a 14 lb load was applied. The area probed was the same relative position in front of the crack and another probe location was positioned to lie within the K-dominated zone. The result of the stress field for the probe location within the K-zone is shown in Figure 37.

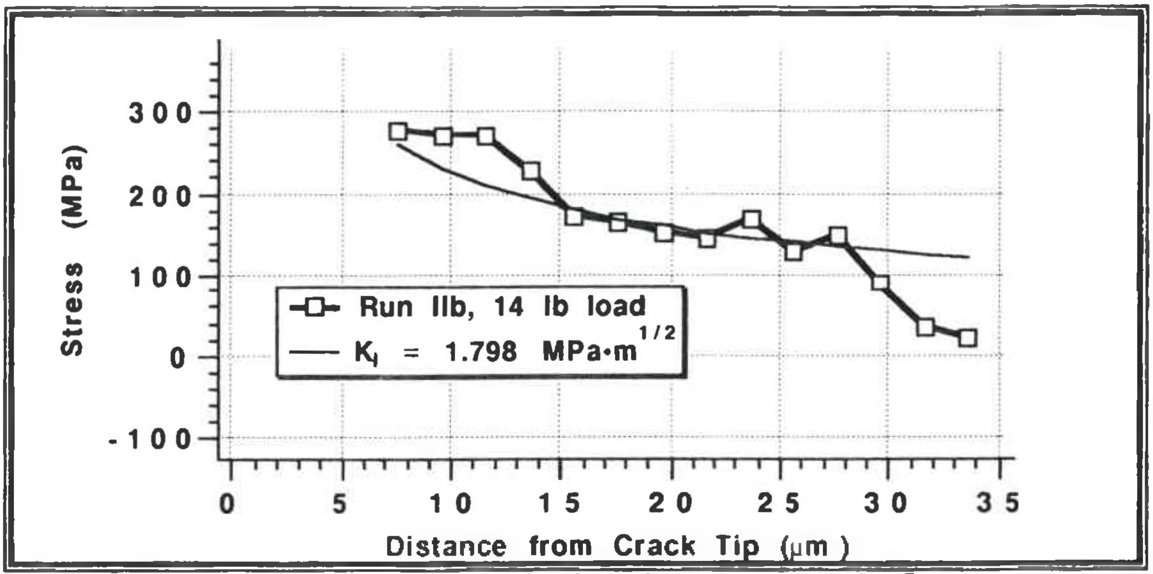

Figure 37: K- dominated zone stress distribution with a stress intensity fit.

The stress field in the K-zone, defined by Equation (21) in Chapter II, was fitted to the data in order to determine the stress intensity factor K_I.

The fit yields a sub-critical stress intensity factor of 1.798 ± 0.13 MPa·m$^{1/2}$. This can be compared with the stress intensity factor due to the applied load, Equation (22) in Chapter II, which yields $K_a = 1.09$ MPa·m$^{1/2}$. From the superposition of stress intensity factors given as

$$K = K_a + K_r + K_m \qquad \text{Ch.II (25)}$$

the non-applied stress factors are found to be,

$$(K_r + K_m) = 0.708 \text{ MPa·m}^{1/2}.$$

Since K_m is not known, K_r cannot be determined. Furthermore, since K_m may be negative[59] then K_r cannot be compared to K_a without further data. Unfortunately, all other runs performed lie within the process zone and so a comparison of (sub-critical) stress intensity factors is not possible.

Figure 38 shows the results of the process zone stress field with a 83.3 MPa (14 lb) bending stress applied (Run IIa) and with the load released (Run IIc). Both runs contain some data points beyond the process zone, but there are not enough points to determine the stress intensity factor. However, the maximum stress values mark the edge of the process zone. The maximum stress values of ~380 MPa appears quite constant between nine and 16 microns in front of the crack tip. Also the maximum stress value for Run IIc is nearly identical at ~400 MPa and as indicated in Chapter II, this represents the yield stress. This is less than the observed maximum stress values of ~480 MPa in Run Ib, before the crack propagated.

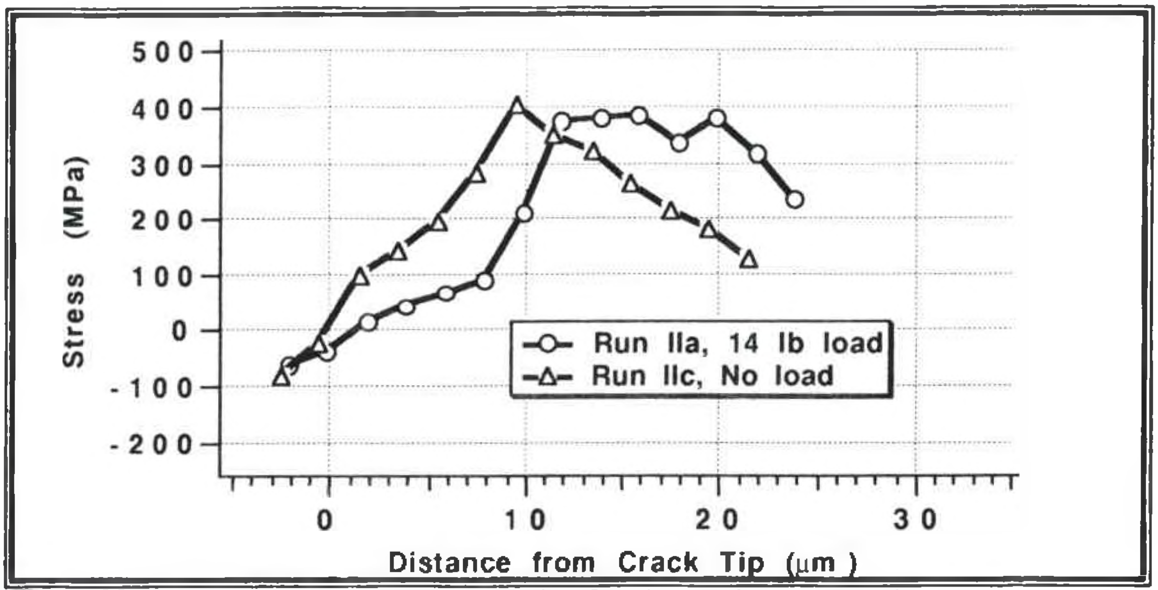

Figure 38: Stress distribution at the crack tip after the crack propagated.

Both plots in Figure 38 indicate a compressive region around the tip similar to crack stresses in Runs Ia, Ib and Ic, although the compressive region in Run IIa does not extend comparatively as far in front of the crack tip. Also, the stress values for Run IIb do not line up well with the stress found in Runs IIa and IIc. The variation in stress values implies errors in the Raman mode shifts observed and/or errors in the exact probe location with respect to the crack tip.

Further comparison of the crack tip stress fields necessitates a removal of these possible sources of error. Concerning an error of the Raman mode shifts, along the y-axis of the stress field plots, the validity is maintained between spectra and runs by the use of the nitromethane Raman reference. Any variation or misalignment of the optics or spectrometer may result in an absolute Raman error, but the relative difference in wavenumbers between the 864 cm^{-1} and the 915 cm^{-1} modes do not vary. Errors in the probe location can be compensated by considering the concept of bridging stresses behind the crack tip.[58] This stress acts to oppose the crack opening stress due to applied load. It is confined to a bridging zone behind the crack tip and is a compressive stress. The distribution of this stress is zero at the crack tip, is maximum behind the crack tip, and is zero much farther behind the crack tip. As mentioned before, the actual crack tip is the location where the stress reverses from compressive (bridging stress) to tensile (process and K-dominated zone). The process zone stresses of Runs Ia, Ib, Ic, IIa and IIc can be shifted so that the crack tip occurs at zero stress. To do this a general quadratic fit was performed on each of the process zone stresses from Runs Ia, Ib and Ic. Because of the similarity of the process zones in Runs Ia,Ib and Ic, a composite quadratic fit was used to fit the process zones of Runs IIa and IIc. The composite was constructed using the average of the linear and quadratic terms from the fits of Runs Ia, Ib and Ic process zone stresses. In each fit no constraint was placed on the x-offset and y-offset parameters which means the maximum bridging stress (y-offset) and the distance behind the crack tip where it is located (x-offset) was determined by the fit. The process zones and the fits are shown in Figures 39 and 40.

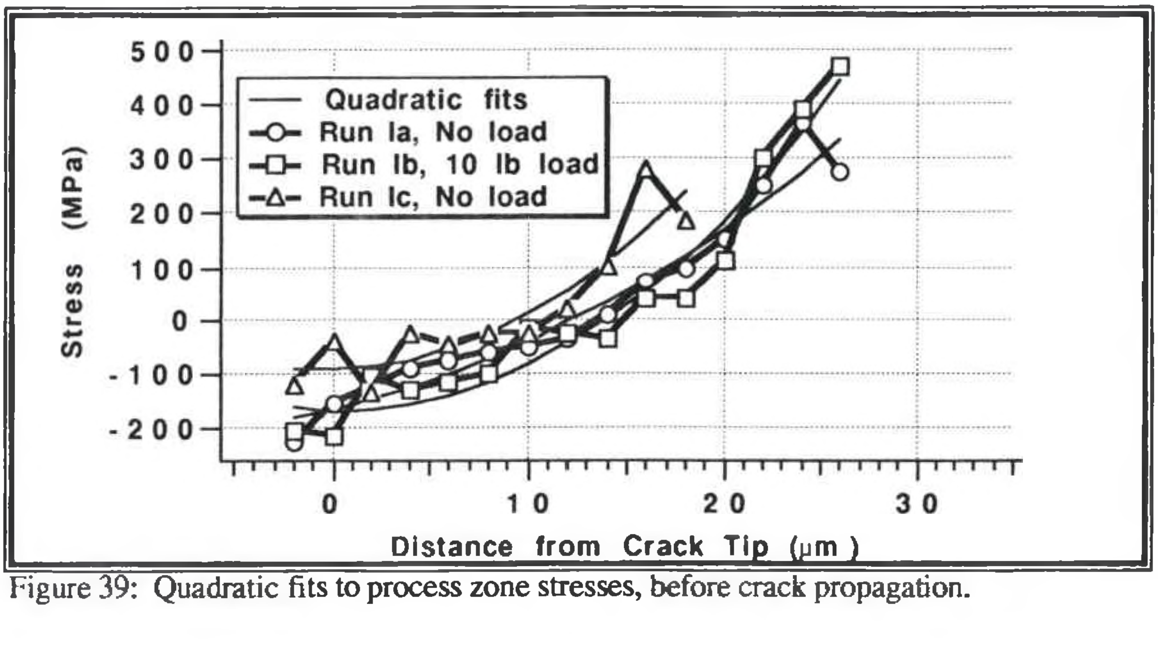

Figure 39: Quadratic fits to process zone stresses, before crack propagation.

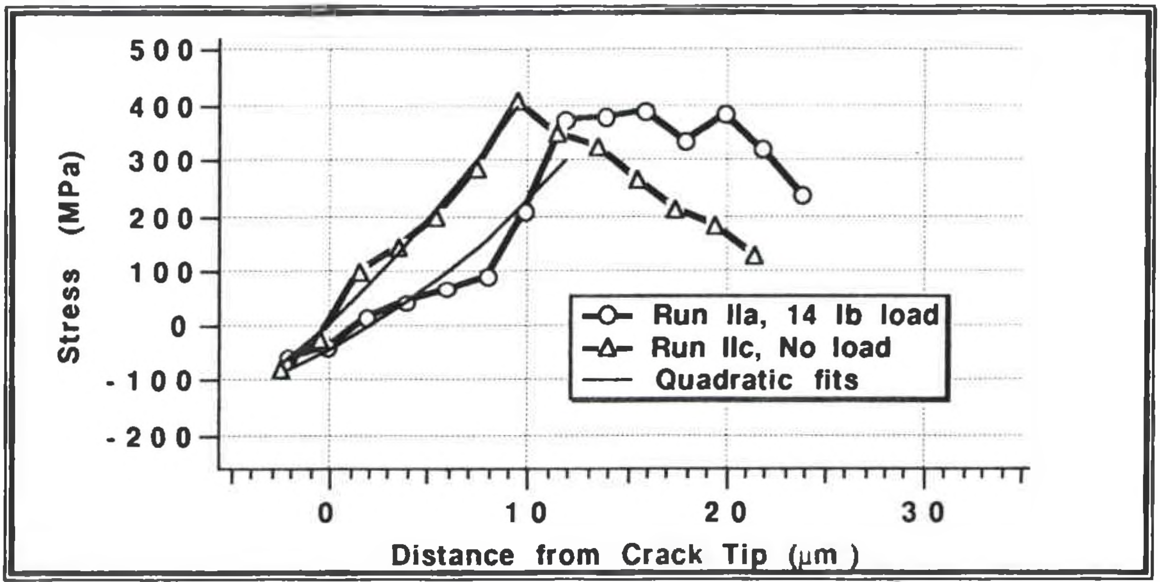

Figure 40: Quadratic fits to process zone stresses, after crack propagation.

The equations generated by the fit are then used to find the shift along the x-axis necessary to align the process zones at zero stress. The coefficients of the quadratic fits and the x-axis shifts are given in Table 4.

Table 4: Coefficients of quadratic fit to process zone stress fields

	$y = ax^2 + bx + c$ (MPa)			x-axis Offset (µm)
	a	b	c	
Run Ia	0.41	8.6	-166	12.2
Ib	0.94	-0.90	-168	13.8
Ic	1.00	0.47	- 93	9.3
Composite	0.78	2.7	-143	
Run IIa	0.78	19.4	-42.2	2.01
IIc	0.78	33.5	10.5	-0.31

The shifted process zone stresses of all runs are plotted in Figure 41. Since Run IIb does not cross the zero stress line, its shift cannot be determined. Yet, the amount of shifting found for Runs Ia, Ib, Ic, IIa, and IIc suggest that there is an additional error involved for Run IIb, the K-zone stress field. If the only error is in the location of the probe, then the placement of the probe on the surface is off by about ten microns, a possible misreading of the marks on the micrometer stage dial.

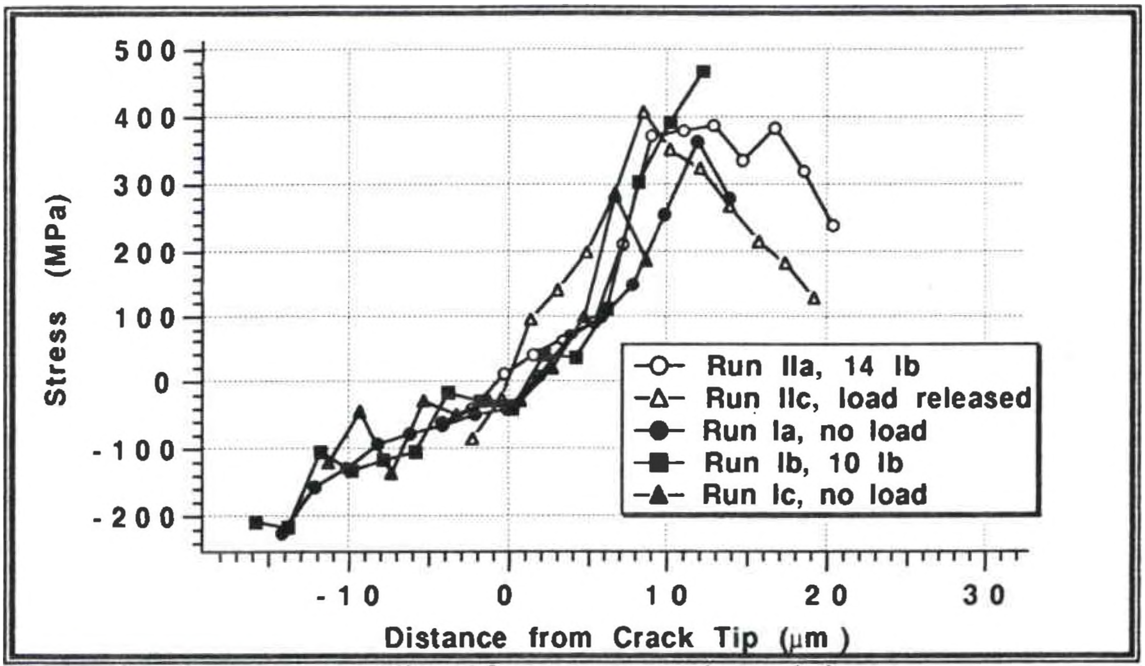

Figure 41: All process zones aligned for zero stress at the crack tip.

The process zone for all runs shown in Figure 41 have a nearly identical slope. The process zone for all runs is 10-16 microns. The process zone is much larger than a single crystallite which suggests that the macrostress is evenly distributed among the crystallites comprising the process zone. Because no data points appear in error, or exhibit an abnormal stress, this suggests the absence of any anamolies like inclusions or boundary phase voids.[36] In comparing Runs IIa and IIc, there appears to be some stress relaxation after the 14 lb load was released. The process zone extends from 9 to 17 microns in front of the crack tip under load. When the load was released, the extended process zone decreased back to eight microns from the crack tip and part of the K-dominated zone was observed. Only the crack system of Run IIa exhibited a stress field which leveled off at the boundary of the process zone and the K-dominated zone. Essentially, the K-dominated zone dropped back about eight microns which indicates the contribution of the stress intensity due to the applied stress K_a on the total subcritical stress intensity K.

Although the process zone stress field does not appear to have shifted significantly before and after the crack propagated, the residual stress intensity due to the indentation has changed. This change can be determined as a percent change using Equation (26) in Chapter II. Since the crack extension is known (209 microns to 270 microns measured tip to tip) the percent change in the K_r factor is

$$\frac{\Delta K_r}{K_r} = -32\ \% \ .$$

This value only has a relative meaning since K_r is unknown. However, the decrease by 32% suggests that K_r has no major effect on the process zone. The decrease also supports the concept that after the crack propagated, the applied stress intensity factor K_a appears to play a more dominate role on the total stress intensity factor K.

CHAPTER VI

CONCLUSIONS AND RECOMMENDATIONS

The main thrust of this work has been to study the stress fields of polycrystalline β-Si_3N_4. At the heart of the studies lies the measurement of the Raman shift of the 864 cm^{-1} mode. The shift is due to strain in the β-Si_3N_4 crystallites and this was used to relate the observed mode shifts with the known stress gradients of a specimen on its side. Quantitative information on this study was used to investigate the strain (stress) fields in front of a crack tip. Additionally, studies were carried out for upgrading the microprobe in the following three areas: 1) Computer-generated ray trace analysis of the astigmatism correction of the spectrometer using a cylindrical lens experimentally studied by Blackshire and Yaney;[12] 2) Introduction and assessment of a holographic edge filter; and 3) Design of a laser spot scanner to increase the range of spatial coverage possible with the microprobe.

Microprobe Upgrades

The measurements rely on the detection capability of the microprobe. The addition of the CCD array greatly reduced the exposure time required for detecting mode shifts and made it possible to simultaneously resolve microscopic segments of the probed surfaces.[12] Although achieving imaging capability with a double spectrometer was accomplished by Blackshire and Yaney[12] there was some uncertainty as to whether the observed performance was optimized. The ray trace analysis performed at the beginning of this thesis work showed that the observed performance was clearly optimized. Moreover, it showed no significant improvement could be achieved with a different cylindrical lens focal length. The optical performance was within the 23 micron size of the pixels over the useful range of the detector; however, it is not clear that the performance will extend over the entire detector area. There was also a need to reduce the exposure time without sacrificing signal-to-noise-ratio which could only be accomplished by suitable filtering of the laser (Rayleigh) line. The addition to the microprobe of a holographic edge filter and using an extended laser line image on the specimen made it possible to resolve two micron segments on the specimen. For this work, the total line image on the specimen was 28 microns which consisted of 14 pixels stripes on the array detector. The analysis of the features of the stress distribution at the crack tip and a ever-present desire to increase the signal-to-noise ratio of the microprobe prompted a change in the illumination scheme. A galvanometer scanner connected to the beamsplitter scans a precisely controlled line on the specimen with a rectangular intensity profile. With the new method, it is possible to probe a line image on the specimen up to 100 microns in length with a time-averaged rectangular intensity profile.

Si_3N_4 Strain Mapping

The measured Raman mode shifts for the Si_3N_4 specimens under flexural stress behaved as expected. This allowed a conversion factor from mode shift to stress to be calculated based on the theoretical stress distribution of the mechanically stressed specimens. For the two specimens measured, the average stress-to-mode-shift ratio was 350 MPa / cm^{-1}. Two specimens of the same material were studied at 80 lb and 100 lb loads. Both produced a conversion factor within 2% of the average. The measurements were conducted on the side of the specimens under flexural stress. A comparison was made of the stress-to-mode-shift ratio with the ratio obtained by Blackshire and Yaney in which similar studies were conducted on the same material on the tensile surface of the specimen. Blackshire's and Yaney's ratio was less which indicated some systematic error was possible. However, because two separate specimens were subjected to different loads for this work, this suggests that the accuracy of the measurements and resulting conversion factor is reasonable. A potential error in the conversion factor could arise if there is some friction between the specimen and the loading rods on the four-point bend fixture.

The Raman mode shifts were recorded at positions in front of the crack tip for various loads to study the stress fields at the crack tip. The conversion factor determined from the previous study was used to calculate stress values from the mode shifts. Two crack systems were studied under applied loads and no load conditions. The first crack system studied was a crack formed by a diamond indent. The same crack was studied after the crack propagated due to applied stress. Three distinct stress zones were observed near the crack tip. The process zone occurred up to 16 microns in front of the crack tip and beyond that the K-dominated zone was observed. A compressive stress zone was observed behind the crack tip due possibly to the bridging or closure stresses.[58] Of the six runs performed, five were located primarily in the process zone stress field. Only one was located completely in the K-dominated zone. The location where the stress reversed from compression to tension defined not only the boundary between the process zone and the bridging stress zone but was also attributed to the actual crack tip location. The position data of the runs in the process zone were corrected to place the crack tip at zero stress. A reasonable sub-critical stress intensity factor was determined for the one run located in the K-dominated zone. A lack of runs at locations in the K-dominated zone prohibited a comparison of sub-critical stress intensity factors between crack systems of this study. The predicted yield stress magnitude occurred at tensile stress values between 380 MPa and 450 MPa for the five runs in the process zone.

The data obtained for the crack studies appears valid for these reasons. Primarily, the stresses followed the trends predicted by the variation on linear elastic fracture mechanics. The yield stress was present in most runs, and for one run (IIa) was constant between 9 and 17 microns in front of the crack tip. The data from the three runs performed on the crack before propagation (Runs Ia, Ib and Ic) did not show any significant discrepancies which shows the good precision of the technique.

The ability of the microprobe to detect strain is apparent in these studies. If the line image is binned together, as was the case for the tension-to-compression study, the strain measured is averaged over the probe length of ~30 microns. If the line image is completely resolved, as was the case for the crack tip studies, the strain can be detected down to two microns. However, all the strain measurements are of the surface grains. Also, the localized strain may be modified by the grain boundary phase. Nonetheless, the technique can reveal much information about the microscopic stress in polycrystalline β-Si_3N_4 and crack tip stresses in particular.

The crack tip stresses of polycrystalline materials have not previously been studied using the strain-induced Raman mode shift technique. There is, therefore, a need for more data and theoretical development. However, based on our understanding at this time, four speculations can be made regarding the data presented herein. The similarity of the observed process zone stress profile suggests that for a given material the process zone of any crack system, regardless of load, will have a similar profile. Only if the load is sufficient to propagate the crack does the process zone change, as in Runs IIa and IIc. Runs Ia, Ib and Ic demonstrate that at sub-critical loads (10 lb) the process zone does not change. This may be a result of the crack propagating through or around high stress sites and arresting in an area free of high stress sites. This neglects any grains with an abnormally high bridging stress which may extend across the walls of the crack.[60] If there are no high bridging stresses then the crack arrests at an equilibrium of bridging stresses behind the crack tip and tensile stresses in front of the crack tip.[61] This appears to be the case with Run IIa.

The bridging stresses located behind the crack tip may be responsible for the compressive stress observed in five of the runs. It is possible that the bridging stresses work to close or heal the crack and thus, over time, visually obscure the crack tip.[62] Therefore, the visually observed crack tip is actually located behind the crack tip. This explains the fact that the measurements of the crack before propagation do not exhibit zero stress values at the crack tip. To compensate for this, the positions of the process zone stress fields were corrected. The x-axis corrections are shown in Table 4. All the measurements of the crack before propagation (Runs Ia, Ib, and Ic) required corrections up to 13 microns while the data for the crack just after propagation (IIa and IIc) needed little or no correction (a few microns).

This concept of a closed crack tip does not consider the existence of a damage zone (cavities between bridging grains) at the crack tip as found in alumina and other nontransforming ceramics.[60,63] Also, Thouless[60] equates the bridging near the tip with the damage zone observed at crack tips and, in essence, defines two crack tip locations, behind and in front of the damage zone. This further complicates the determination of the true crack tip and so future studies will depend on the definition of the true crack tip. Future studies of stress very near to the crack tip may offer additional insight into the role of the bridging stresses.

The process zone size was found to be 10-16 microns which is larger than the grain size. This not only shows the that the macrostress is evenly distributed, but because the process zone size does not vary significantly, this indicates the ability of the grain boundary phase to withstand high stress states which naturally occur at crack tips. It is possible, then to infer the contribution of the boundary phase on the stress intensity by comparing process zone sizes and yield stress magnitudes with similarly structured ceramics.

Future experiments should explore the three stress zones to further characterize their existence and size for various crack systems. In particular, the line image could be lined up perpendicular to the crack in order to map the entire area around the tip and more runs performed may help to quantify the stress intensity factors. This may offer some connection to the R-curve behavior of ceramics.[63] In addition to measuring the stresses at the crack tip, the plastic region under the indent can also be studied. By comparing the stress values of a probed area on the specimen with a scanning electron micrograph of the same area, the effect of the grain boundary phase or the stress in an individual grain could be investigated.

The accuracy of the microprobe to image the probe line on the detector needs to be improved since this is of great importance to determining stress intensity factors. One of the problems for this work was determining the exact position of the line image at the array detector. An external reference is necessary so that one pixel on the detector corresponds to a known location on the specimen surface. Also, the error in the slight movements of the detector need to be alleviated. The addition of the galvanometer will help because precise focusing and positioning of the laser beam is possible.

The future of Raman microprobe analysis of polycrystalline ceramics such as silicon nitride looks very bright. With the galvanometer addition proposed in this work, the imaging accuracy will be increased to provide quantitative analyses of crack tip stresses or other microscopic strain features.

REFERENCES

1. J. Brandmüller, and W. Kiefer, "Fifty Years of Raman Spectroscopy", p.3, 1978.

2. Ibid., p.3. From ref number 12.

3. M. Tobin, Laser Raman Spectroscopy, Wiley-Interscience, New York, (1971), p.3.

4. H. G. Edwards, D. W. Farwell, M. R. Seaward, C. Giacobini, "Preliminary Raman Microscope Analysis of a Lichen Encrustation Involved in the Biodeterioration of Renaissance Frescoes in Central Italy." International Biodeterioration, v.27 n.1, (1991), p. 1-9.

5. I. Siebinga, F. F. de Mul, G. F. Vrensen, J. Greve, "Spatially Resolved Water Concentration Determination in Human Eye Lenses Using Raman Microspectroscopy." Lasers in Biophysics and Biomedicine Proceedings of SPIE. v.1403 pt. 2. p. 746-748.

6. E. S. Etz, "Raman Microprobe Analysis: Principles and Applications," Scanning Electron Microscopy, (1979), p. 67.

7. M. Wager, Design and Development of a Laser Raman Microprobe, M.S. Thesis in Electro-Optics, December, 1985.

8. M. Lander, S. Pruchnic, P. Yaney, "Application of Laser Raman Macro- and Microprobes Using Cylindrical Optics to the Study of Zirconia Ceramic Materials," Bull. Am. Phys. Soc., No. 32, p. 2163, (1987).

9. S. Pruchnic, M. Lander, J. Schneider, P. Yaney, "Development of a Raman Spectroscopy Facility for Quantatative Analyses of Material," Bull. Am. Phys. Soc., No. 32, p. 1293, (1987).

10. P. Fettig, P. Yaney, :"Development of 2-D Characterization of Ceramics Using Raman Microprobe Spectroscopy," Bull. Am. Phys. Soc., No. 33, P. 1800, (1988).

11. K. Jennings, P. Yaney, "Grain Structure Studies of Silicon Carbide Ceramics Using a Laser Raman Microprobe," Bull. Am. Phys. Soc., No. 35, p. 51, (1990).

12. J. Blackshire and P. Yaney, " Studies of Spatial Variations in Crystalline Orientation Near a Fracture Edge of Advanced SiC Ceramics Using a Laser Raman Microprobe," Spring Meeting of Ohio Section of APS, Dennison Univ., 1990.

13. D. Richerson, Modern Ceramic Engineering, Marcell Dekker, Inc. New York, (1982), p. 78.

14. J. Loader, Basic Laser Raman Spectroscopy, Heyden & Son Ltd. London, (1970), from reference number 2.

15. E. S. Etz, op cit, p. 68.

16. P. Sherwood, Vibrational Spectroscopy of Solids, Cambridge University Press, London, (1972), p. 2.

17. J. Jackson, Classical Electrodynamics, Wiley, New York, (1962), p. 109.

18. M. Tobin, op cit, p. 6.

19. G. Hertzberg, Molecular Spectra and Molecular Structure, part II: Infrared and Raman Spectra of Polyatomic Molecules, D. Van Nostrand Company, Inc., New York, (1945), p. 67.

20. M. Tobin, op cit, p. 16.

21. P. Milonni and J. Eberly, Lasers, Wiley, New York, (1988), p. 50.

22. P. Sherwood, op cit, p. 3.

23. S. Nakashima and M.Hangyo, "Characterization of Semiconductor Materials by Raman Microprobe," IEEE Journal of Quantum Electronics, Vol. 25, No. 5, (1989), p. 965.

24. J. Rydzak and W.R. Cannon, "Fourier Transform Infrared Microscopy Method to Determine Stress in Sapphire," Journal of the American Ceramic Society, Vol. 72, No. 8, p. 1559, from Ref. 13.

25. D. Richerson, op cit, p. 77.

26. H. Shen and F. Pollak, "Raman Study of Polished-Induced Strain in <100> GaAs and InP," Applied Physics Letters, Vol. 45, No. 6. (1984), p. 694.

27. D. Richerson, p. 126.

28. N. Wada, S. Solin, J. Wong and S. Prochazka, " Raman and IR Absorption Spectroscopic Studies on α,β and Amorphous Si_3N_4," Journal of Non-Crystalline Solids, 43, (1983), pp. 7-13.

29. R. Grün, "The Crystal Structure of β-Si_3N_4; Structural and Stability Considerations Between α- and β-Si_3N_4." Acta Crystallographica, Vol. B35, (1979), p. 800-804.

30. N. Wada, op cit, p. 9.

31. A. Takase and E. Tani, "Low-frequency Raman spectra of sintered Si_3N_4 under gas pressure," Journal of Materials Science Letters, Vol. 6, (1987), p. 607.

32. J. Blackshire, "Raman Microprobe Studies of Mechanically Stressed Si_3N_4 Ceramic Materials using Charge-Coupled Device Detection." M.S. Thesis, University of Dayton, (1991).

33. H. Saliba, L. Chuck, N. Hecht, "high Temperature R-Curve Determination of a HIP'ed Silicon Nitride", Ceramic Engineering Science Proceedings, Vol. 12, No. 7-8, pp. 1418-1436, (1991).

34. P. Yaney, private communication.

35. A. Moulson, "Reaction-bonded silicon nitride: its formation and properties." Journal of Materials Science, No. 14, (1979), p. 1044.

36. L. Chuck, S. Goodrich, N. Hecht, and D. McCullum, "High-Temperature Tensile Strength Stress Rupture Behavior of Norton/TRW NT-154 Silicon Nitride," Ceramic Engineering Science Proceedings, 11[7-8], (1990), pp. 1007-1027.

37. J. Shigley, Mechanical Engineering Design, 3rd. edition. McGraw-Hill, Inc. 1977, p. 45.

38. D. Richerson, op cit, p. 93.

39. S. Rolfe and J. Barsom, Fracture and Fatigue Control in Structures, Prentice-Hall, Inc., New Jersey, 1977, p.15.

40. A. Haerle, W.R. Cannon, M. Denda, "Direct Measurement of Crack Tip Stresses," Journal of the American Ceramic Society, Vol. 74, No. 11, (1991), p. 2897.

41. R. Cook and G. Pharr, "Direct Observation and Analysis of Indentation Cracking in Glasses and Ceramics," Journal of the American Ceramic Society, Vol. 73, No. 3, (1990), p. 788.

42. S. Rolfe, op cit, p. 39, from reference 14, G. Irwin.

43. S. Rolfe, op cit, p. 18.

44. C.J. Fairbanks, B. Lawn, R. Cook, Y. Mai, "Microstructure and the Strength of Ceramics", from Fracture Mechanics of Ceramics, Vol. 8, R. Brandt, ed., Plenum Publishing Corporation, 1986, pp. 23-37.

45. S. Rolfe, op cit, p. 58.

46. Princeton Instruments, Inc., CSMA Manual, Ver. 1.3, Princeton Instruments, New Jersey, (1990).

47. Stellar Software, Beam Four Optical Ray Tracer, Stellar Software, Berkeley, Ca., (1991).

48. A. Thelen, Design of Optical Interference Coatings, McGraw-Hill, 1989, p. 45.

49. C. Rich and D. Cook, " Lippmann Volume Holographic Filters for Rayleigh Line Rejection in Raman Spectroscopy", Proceedings from SPIE, Practical Holography V, Vol. 1461, (1991).

50. Physical Optics Corporation, Holographic Edge Filters, Physical Optics Corporation, Torrance, Ca. (1991).

51. Corning Laboratory Glassware, Color Glass Filters, Corning, New York, (1965).

52. Crystal Technology, Inc., Acousto-Optics and Electro-Optic Products, Mini Catalog, Crystal Technology, Inc., Palo Alto, Ca. (1991).

53. General Scanning, Inc., G300 Series Galvanometer Scanner, General Scanning, Watertown, Mass. (1990).

54. General Scanning, Inc., private communication.

55. J. Blackshire, op cit.

56. A. Haerle and others, op cit, p. 2899. Similar results cited in reference 15 of this article.

57. Dr. H private comm

58. C. Hsueh and P. Becher, "Evaluation of Bridging Stress from R-Curve Behavior for Nontransforming Ceramics", Communications of the American Ceramic Society, Vol. 71, No. 5, C-234 - C-237, (1988).

59. C. J. Fairbanks and others, op cit, p. 28.

60. M. Thouless, "Bridging and Damage Zones in Crack Growth", Journal of the American Ceramic Society, Vol. 71, No. 6, p. 408, (1988).

61. S. Choi, J. Salem, and W. Sanders, " Estimation of Crack Closure Stresses for In Situ Toughened Silicon Nitride with 8 wt% Scandia", Journal of the American Ceramic Society, Vol. 75, No. 6, p. 1508, (1992).

62. D. Broek, Elementary Engineering Fracture Mechanics, Kluwer Academic Publishers, Dordrecht, 1986, p. 126.

63. P. Swanson, C. J. Fairbanks, B. Lawn, Y. Mai, and B. Hockey, "Crack-Interface Grain Bridging as a Fracture Resistance Mechanism in Ceramics: I, Experiamental Study on Alumina", Journal of the American Ceramic Society, Vol. 70, No. 4, p. 279, (1987).